Posted on 25 Mar 2024 — The copyright holder is the author/funder. All rights reserved. No reuse without permission. — https://doi.org/10.22541/essoar.171137003.34080490/v1 — This is a preprint and has not been peer-reviewed. Data may be preliminary.

Obtaining the Equation of State for Multiphase Iron under Earth's Core Conditions using Bayesian Statistics

Run Wu[1], Shikai Xiang[1], Yi Sun[1], Yunting Xian[1], Yin Luo[1], and Feifan Dai[2]

[1]National Key Laboratory for Shock Wave and Detonation Physics, Institute of Fluid Physics, China Academy of Engineering Physics
[2]State Key Laboratory of Advanced Technology for Materials Synthesis and Processing, Wuhan University of Technology, Wuhan 430070, China

March 25, 2024

Abstract

Iron, a principal element of Earth's core, is vital for understanding the thermodynamic properties of this region. The accuracy of iron's equation of state (EOS) is crucial, yet experimental uncertainties significantly impact the EOS parameters. By employing Bayesian statistics and Markov Chain Monte Carlo (MCMC) simulations, we have quantified these uncertainties. Our approach introduced a straightforward yet effective method to calculate the probability of phase boundary data. The resulting EOS reliably reproduces a variety of experimental datasets, including phase boundary experiments, static pressure measurements under various conditions, shock wave data, and sound velocity under different states. Using 100 sets of posterior parameter samples, our predictions indicate that the density deficit in Earth's outer core ranges approximately from 8.7% to 9.7%. Additionally, the inferred geodynamo power output from latent heat release during the cooling and solidification process of Earth's inner core is estimated to be between 0.458 and 6.002 terawatts.

Obtaining the Equation of State for Multiphase Iron under Earth's Core Conditions using Bayesian Statistics

Run Wu[1], Shikai Xiang[2*], Yi Sun[2*], Yunting Xian[3], Yin Luo[4], Feifan Dai[5]

National Key Laboratory of Shock Wave and Detonation Physics, Institute of Fluid Physics
China Academy of Engineering Physics, Mianyang 621999, China

Key Points:

- Under the framework of Bayesian statistics, the uncertainty of parameters in the multiphase equation of state of iron is quantified.
- A simple and accurate probability method for calculating the phase boundary data of iron is proposed
- EOS estimates Earth's outer core density deficit at 8.7%-9.7% and geomagnetic power output from inner core cooling at 0.458-6.002 TW.

Plain Language Summary

Iron constitutes the primary element of the Earth's core, and understanding its thermodynamic properties is essential. The equation of state for iron is crucial for these insights. However, the inherent uncertainties in experimental data can significantly impact the parameters that define iron's equation of state. To address this, we employed Bayesian statistics coupled with Markov chain Monte Carlo (MCMC) simulations, allowing us to quantify the uncertainties surrounding these parameters. In our approach, we developed a straightforward yet effective method to calculate the probability associated with phase boundary data during the simulation process. The outcomes from our simulations yielded an equation of state that precisely mirrored a variety of experimental data sets, including phase boundary measurements, static pressure readings under diverse conditions, shock wave observations, and acoustic velocity determinations across different states. Armed with 100 posterior parameter samples, we honed in on the Earth's outer core density deficit, predicting it to fall within a range of approximately 8.7% to 9.7%. Furthermore, we estimated the geodynamo power output, generated by the latent heat released during the cooling and solidification of the Earth's inner core, to be between 0.458 and 6.002 terawatts.

Corresponding author: Shikai Xiang, `skxiang@caep.cn`

Corresponding author: Yi Sun, `ssunyyi@163.com`

Abstract

Iron is the primary constituent element of Earth's core, and its equation of state plays a pivotal role in understanding the thermodynamic properties of the core. However, uncertainties in experimental data have significant effects on the parameters within the iron equation of state. Using Bayesian statistical analysis coupled with Markov chain Monte Carlo (MCMC) simulation methods, we quantified the uncertainties in the equation of state parameters. During the simulation process, we proposed a simple yet efficient computational method for determining the probability of phase boundary data. The equation of state we obtained accurately reproduces various experimental data, including phase boundary experiments, static pressure data under different conditions, shock wave data, and sound velocity data at different states. With 100 posterior parameter samples, we predict that the density deficit of Earth's outer core falls within a range of approximately 8.7% to 9.7%, and the geodynamo power output due to latent heat release during the cooling and solidification of Earth's inner core is estimated to be between 0.458 to 6.002 terawatts.

1 Introduction

The Earth's core is primarily composed of iron, with minor inclusions of lighter elements such as nickel, sulfur, and oxygen (Li & Fei, 2014; Hirose et al., 2021). Iron significantly influences the propagation of seismic waves, and by meticulously analyzing these waves in conjunction with the equation of state for iron, we can deduce the spatial distribution of iron and other light elements within the core (Dziewoński & Anderson, 1981; Ichikawa et al., 2014; Kuwayama et al., 2020), thus revealing its complex structure. Additionally, the formation of the Earth's magnetic field is linked to the flow in the electrically conductive liquid outer core, a process driven by thermal convection (Labrosse, 2014; Singh et al., 2023a). Therefore, an in-depth study of the physical properties of iron under core conditions is of irreplaceable importance for elucidating the generation mechanism and evolutionary history of the Earth's magnetic field. Overall, investigating the thermodynamic behavior of iron under extreme high pressure is crucial for addressing fundamental questions about the Earth's core structure and dynamics; the precise equation of state for iron is key to these research topics.

Traditional methods for determining parameters in the equation of state model may introduce inaccuracies due to data uncertainty. Recognizing this is particularly important when studying the role of iron in the Earth's core. Although past studies have explored the equation of state for iron experimentally, they often did not utilize Bayesian data analysis, which incorporates prior knowledge and data uncertainty. Bayesian methods provide a probability distribution of parameters, continually updating it with new data, thus enhancing simulation accuracy and deepening our understanding of Earth's interior processes. In the Bayesian framework, conventional approaches determine phase transition boundaries based on Gibbs free energy but require complex numerical computations. To simplify this, Lindquist and Jadrich (Lindquist & Jadrich, 2022) introduced a model that categorized phase diagram data effectively. We focus on solving the phase boundary problem quickly and accurately, avoiding numerical inversion while adhering to the principle of equal Gibbs free energy between phases, significantly improving efficiency and accurately reproducing phase boundaries.

2 Simulation Methodology and Details

In data analysis, Bayesian statistics and Markov chain Monte Carlo (MCMC) methods are closely coupled to effectively manage uncertainty. Bayesian inference combines prior knowledge with new data to generate probabilistic distributions of model parameters, offering a more holistic perspective on uncertainty than traditional methods. In the study of multiphase equations, leveraging phase boundary data to constrain model parameters is an efficient approach, typically involving measurements of pressure (P) and temperature (T). Conventional methods are based on the principle of Gibbs free energy equilibrium and require numerical inversion to determine the relationship between P and T (P(T) or T(P)) for subsequent MCMC calculations of system state probabilities. However, this computational process is costly when dealing with complex inverse relationships between P and T. To enhance efficiency, Lindquist and Jadrich (Lindquist & Jadrich, 2022) innovatively transformed phase diagram data into a probability classification problem in their study of carbon's equation of state, achieving notable success. We also propose a simplified method that avoids complex numerical inversion while maintaining equal Gibbs free energy at phase boundaries. Specifically, we use probability estimates derived from indirect measurements to handle phase boundaries, rather than direct measurement-based probability computations, thus obtaining the P-T relationship without the need for numerical inversion, significantly improving computational efficiency. The details of our innovative phase boundary handling technique and parameter quantification can be found in the supplementary materials Text S2 and Text S3.

3 Multi-phase state equation of iron

In this study, we utilized the Python-emcee library (Foreman-Mackey et al., 2013) for parameter sampling, coupled with Python-numpy (Harris et al., 2020) for efficient data manipulation, and leveraged Python-seaborn (Waskom, 2021) to create visualizations, thereby facilitating in-depth analysis and intuitive representation of the data. Employing Bayesian theory and MCMC sampling techniques, we obtained a set of samples for the 40-dimensional parameters within the model (Dorogokupets, 2017). Through marginalization, we derived the marginal posterior distributions for each parameter, presenting them graphically to illustrate individual parameter behavior. Additionally, we computed and plotted a correlation matrix to visually depict inter-parameter relationships. Furthermore, based on 1000 sets of sample parameters, we estimated the parameter values corresponding to the maximum posterior probability (MPP). Detailed results can be found in the supplementary information Text S4.

The Fig.1 shows the phase diagram obtained using Maximum Posterior Probability (MPP) for parameter estimation. Along the isotherm at 300K, we calculate the bcc-hcp phase transition pressure to be 16.9 GPa. At a pressure of 0.1 MPa, the transformation temperatures from bcc(a) to fcc and from bcc(delta) to fcc are calculated to be 1190 K and 1611 K, respectively, with the melting point reaching 1801 K. We further computed the triple points where the bcc-fcc-liquid triple point is located at 6.0 GPa and 1994 K, the bcc-fcc-hcp triple point at 11.6 GPa and 774 K, and the fcc-hcp-liquid triple point at 109.5 GPa and 3698 K. Near the fcc-hcp-liquid triple point, our calculated phase boundary lines agree with the experimental data of Anzellini et al (Anzellini et al., 2013) and Morard et al (Morard et al., n.d.), but there is a discrepancy with the data of Sinmyo et al (Sinmyo et al., 2018). This mismatch may arise because our simulation dataset only included Morard's experimental data. In the high-pressure region, our calculated melting line for the hcp phase aligns with data based on ab initio free energy calculations (Alfè et al., 2002) and experimental data obtained by Li et al (Li et al., 2020). Additionally, the figure depicts the shock Hugoniot within the hcp phase, plotted using 100 sets of parameters, represented by thick black lines. The calculated shock curve intersects the melting line at the shock-induced melting point, which is located at 215 GPa and 5100 K. (The relationship between the shock wave and particle velocity used here is based on research by Brown (Brown et al., 2000).) .From the overall results, our calculated outcomes can accurately reproduce the phase boundary data and the shock Hugoniot within the hcp phase.

The Fig.2 displays the deviations between the pressure values calculated using MPP parameters for the various phases of iron (bcc, fcc, hcp, liquid) and the reference datasets.

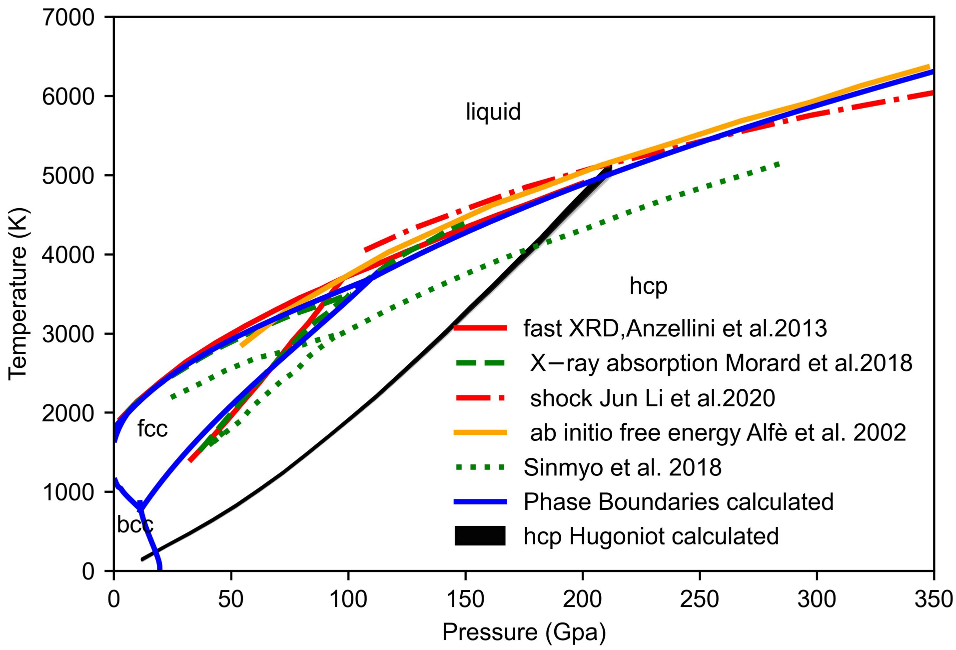

Figure 1. The figure presents a comparison of the calculated phase boundaries for iron obtained using maximum a posteriori parameter estimates against the reference boundary data(Anzellini et al., 2013; Morard et al., n.d.; Li et al., 2020; Alfè et al., 2002; Sinmyo et al., 2018). The black shaded area represents the shock curves within the hcp phase, computed using 100 sets of parameters; the relationship between the shock wave and particle velocity employed here is sourced from Brown (Brown et al., 2000).

.

For the Fe-bcc phase, based on experimental data (Zhang & Guyot, 1999; Dewaele et al., 2015; Dewaele & Garbarino, 2017; Liu et al., 2013; Shibazaki et al., 2016), the maximum deviation of our calculated results is less than 2 GPa. In the Fe-fcc phase, the maximum discrepancy between our computed pressure data and the experimental pressure data does not exceed 5 GPa (Nishihara et al., 2012; Shibazaki et al., 2020; Funamori et al., 1996; Anzellini et al., 2013; Komabayashi & Fei, 2010). Regarding the Fe-hcp phase, except for one set of anomalous data points (Tateno et al., 2010), the deviations of other data (Ohtani et al., 2013; Shahar et al., 2016; Sakai et al., 2014; Komabayashi et al., 2009; Yamazaki et al., 2012; Anzellini et al., 2013; González-Cataldo & Militzer, 2023) from our calculations are mostly within 10 GPa. However, some experimental data for the liquid phase (Kuwayama et al., 2020) show significant differences with the calculated results, which is likely due to substantial experimental errors. These experimental data were measured at multiple temperatures, not under isothermal conditions, and due to the density of the data, it is difficult to clearly label each temperature point on the graph.

The Fig.3 presents a comparison between the calculated shock-experiment-based pressures and the actual experimental measurements. Our calculations indicate that the onset of the shock melting curve for hcp iron occurs at a pressure of 215 GPa. However, the majority of empirical evidence suggests that the actual shock melting pressure is around 220 GPa. Therefore, Fig.3(a) focuses on the shock pressure range below 220 GPa, illustrating the deviation between the calculated shock pressure data and the experimentally determined pressure values within this range. As can be seen from the figure, these deviations are kept within 5 GPa, demonstrating a high degree of consistency between the our calculated results and experimental observations.To further understand the behavior of iron under extreme conditions, particularly in the fully molten state, Fig.3(b) provides a detailed comparison between computational and experimental data within the dynamic high-pressure range of 260 to 480 GPa. In this higher pressure interval, most of the data deviations are still maintained below 10 GPa, indicating that even under very high dynamic pressures, our computational data maintains good agreement with the experimental data (Brown & Mcqueen, 1986; Brown et al., 2000; W. W. Anderson & Ahrens, 1994; Li et al., 2020), thereby validating the accuracy and reliability of our computational results. Synthesizing these findings, our equations of state obtained through MPP parameter estimations are capable of effectively replicating the pressure characteristics of iron across a considerable range.

The Fig.4(a) demonstrates that at room temperature conditions (300 K), the calculated bulk wave speeds in the hexagonal close-packed (hcp) structure across various pressures (30-170 GPa) are higher relative to Murphy's experimental data (Murphy et al., 2013), yet within this pressure range, we also identified that Ohtani's longitudinal wave speed experimental data (Ohtani et al., 2013) are consistently higher than Murphet's measurements. Fig.4(b) shows that within this temperature range, our computed sound velocity data exhibit good agreement with Kuwayama's experimental results (Kuwayama et al., 2020) from High-pressure inelastic x-ray scattering (IXS) measurements of liquid iron. Moreover, when comparing our shock-induced high-pressure acoustic speeds to the findings of Anderson's research (W. W. Anderson & Ahrens, 1994), our calculations reveal a maximum deviation of less than 6.6%, thus confirming the consistency and accuracy of our work.

Furthermore, in the supplementary material Text S5 section, this study compares a series of experimental measurements of physical properties with the results calculated from 100 parameter samples derived from posterior distribution sampling. Our computational findings indicate that the heat capacity of the body-centered cubic (bcc) structure is largely consistent with the experimental data reported by Desai (Desai, 1986). However, at the Curie temperature of 1043 K, the experimentally measured heat capacity significantly exceeds our computational results, which may be attributed to an insufficient model description of the ferromagnetic transition process. Regarding the ther-

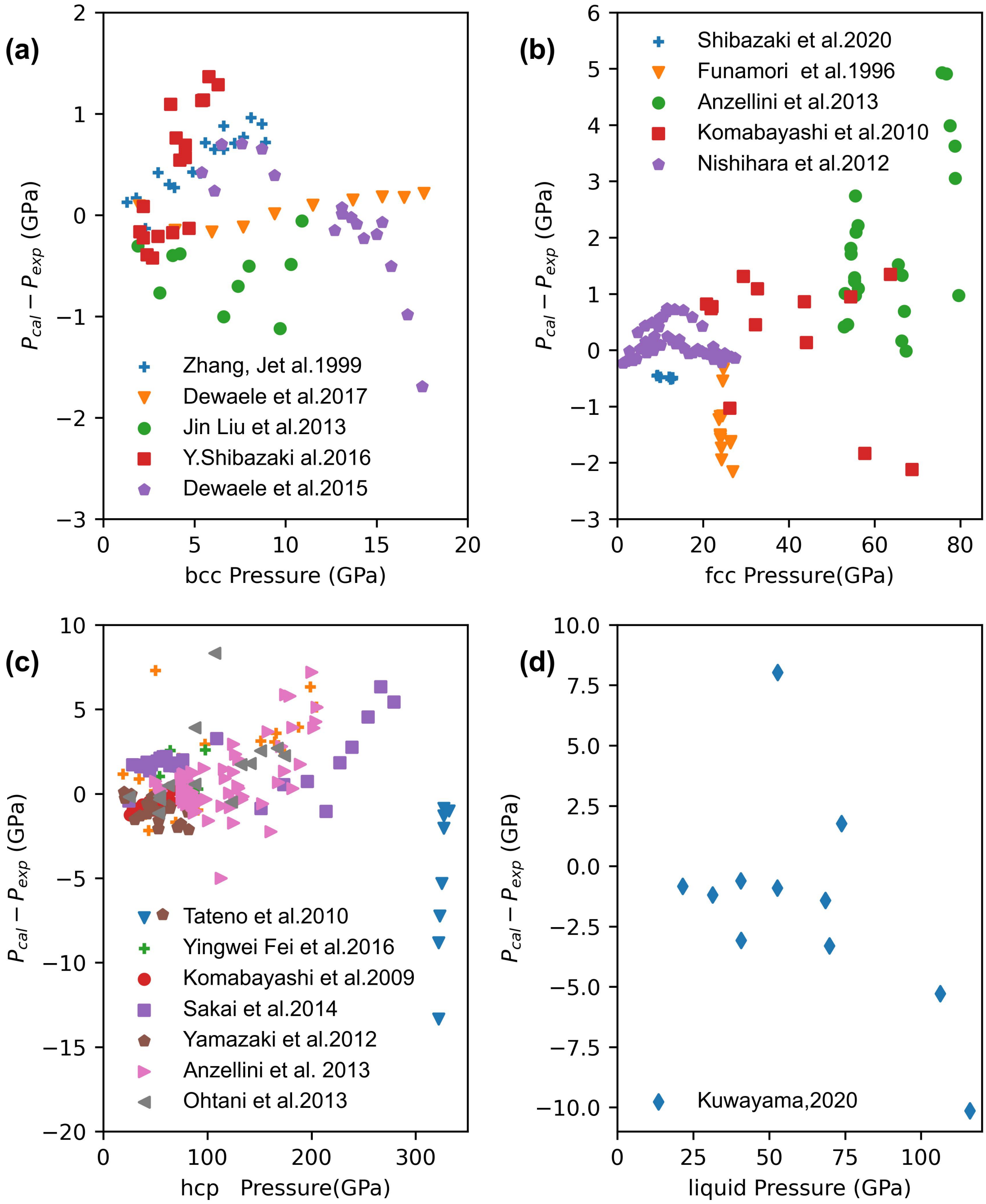

Figure 2. The Fig.2 illustrates the discrepancies between the pressure values computed utilizing MPP parameters applied to various phases of Iron - bcc (a), fcc (b), hcp (c), Liquid (d) - and corresponding reference static high pressure data sets.

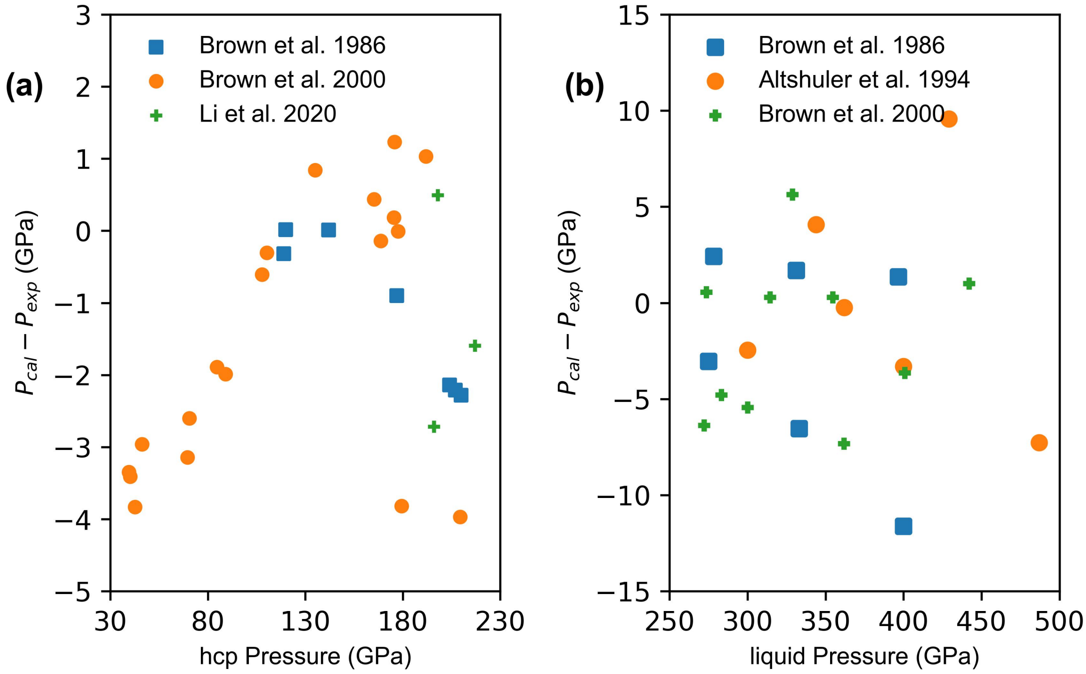

Figure 3. The picture we use MPP parameters estimation to calculate the differences between the computed dynamic high-pressure data for the hcp phase and the liquid phase, and compare them with the corresponding shock experimental data (Brown & Mcqueen, 1986; Brown et al., 2000; W. W. Anderson & Ahrens, 1994; Li et al., 2020).

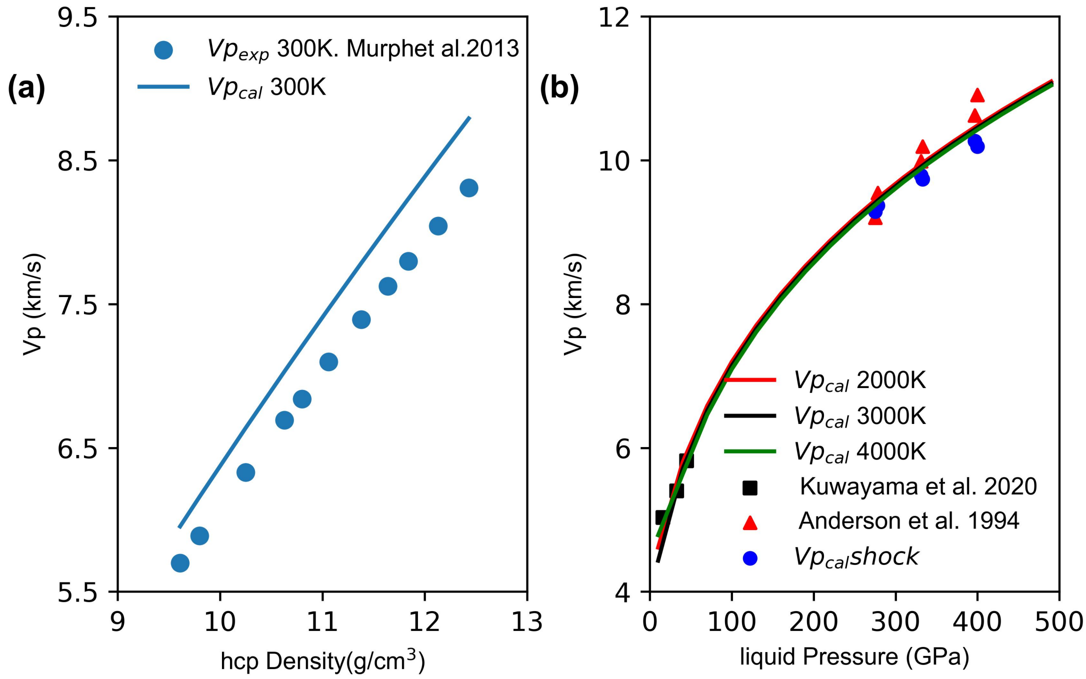

Figure 4. In figure (a), the blue solid line indicates the bulk sound speed of hcp-iron at 300K as calculated by us, and the corresponding blue dots represent experimental data from Murphy (Murphy et al., 2013).In the figure (b), solid lines show our calculated sound speeds at 2000K, 3000K, and 4000K. Black squares are IXS experimental data (Kuwayama et al., 2020); red triangles, shock experiment data (W. W. Anderson & Ahrens, 1994); and blue circles, corresponding shock calculation results.

mal expansion coefficient of iron in bcc and face-centered cubic (fcc) structures, our calculations are in agreement with the experimental data from Dorogokupets's supplementary materials (Dorogokupets, 2017) at lower temperatures; however, at higher temperatures, the computed values are slightly below the experimental observations, possibly due to inadequate experimental constraints applied during the simulation phase. Concerning the isothermal pressure curves of solid phases, our computational results demonstrate that the pressure curves for bcc-Fe at 15 K and 300 K, as well as fcc-Fe at 1073 K and 1273 K, and hcp-Fe at various temperatures, closely match the experimental data (Dewaele & Garbarino, 2017; Liu et al., 2013; Nishihara et al., 2012; Fei et al., 2016). Similar to the heat capacity calculations, the uncertainty range of the isothermal pressure curves is relatively small.

Overall, by utilizing Bayesian statistical theory and MCMC sampling methods, we have systematically obtained the uncertainties of the parameters in iron's equation of state. The simulation results effectively model the diverse behaviors of iron under various conditions of pressure, volume, and temperature, including heat fusion and thermal expansion at ambient pressure as temperatures change, pressure variations at different temperatures, and performance during shock experiments and phase boundary transitions. We achieved equation of state predictions for pressures that cover the range of the Earth's core, with subsequent presentation of our predictions for the thermodynamic properties of the Earth's core to follow.

4 Applications under the Earth core conditions

To accurately quantify certain thermodynamic properties of the Earth's core, we selected 100 sets of sample parameters to assess the uncertainty range in predicted physical quantities introduced by calibration data errors through simulation calculations.

In the simulation study, we have conducted calculations on the melting characteristics of pure iron under conditions at the Earth's Inner Core Boundary (ICB), where at a pressure of 330 GPa, the theoretical melting temperature range for pure iron is between 5997 K and 6262 K. However, the actual melting temperature in the core might be lower due to the presence of lighter elements. To validate these computational results against geological experimental data, we plotted the density(ρ), sonic velocity(V_P), and shear modulus(K_S) of liquid pure iron at various temperatures (4000 K, 5000 K, and 6000 K) under ICB pressure, comparing them with data from the Preliminary Reference Earth Model (PREM) (Dziewoński & Anderson, 1981). The relevant details are shown in the Fig.5. The solid-liquid phase transition temperatures (at the CMB) computed by us spanned intervals of (2928 K-3086 K), (3621 K-3795 K), and (4297 K-4479 K). When setting T_{ICB} at 5000 K, this upper limit approximates the 3800 K proposed by Brown and McQueen in 1986 (Brown & Mcqueen, 1986), as well as the 3739 K given by Stacey and Davis in 2004 (Stacey & Davis, 2004). Adopting a value of 4676 K yields a CMB temperature range of (3398 K-3568 K), which aligns closely with Anderson's 3637 K and Ichikawa's 3585 K (Ichikawa et al., 2014).

Assuming T_{ICB} to be 5000 K, the estimated densities of liquid iron at the CMB and ICB conditions are respectively (10.854 g/cm^3- 10.786 g/cm^3) and (13.226 g/cm^3 - 13.348 g/cm^3). Moreover, the graphs reveal that both the sonic velocity and shear modulus exhibit relatively low sensitivity to temperature changes; our computations show that the outer core's values in these two physical parameters are nearly consistent with PREM data, with small discrepancies in sonic velocity. The figures also demonstrate that the difference in density between solid and liquid iron $\Delta\rho_{solid}$ at the ICB is less than the density change resulting from internal state variations within liquid iron $\Delta\rho_{liquid}$, suggesting compositional differences between the inner and outer cores. Nevertheless, the calculated density deviation range for the outer core (8.7% to 9.7%) provides a strong constraint on the content of light elements.

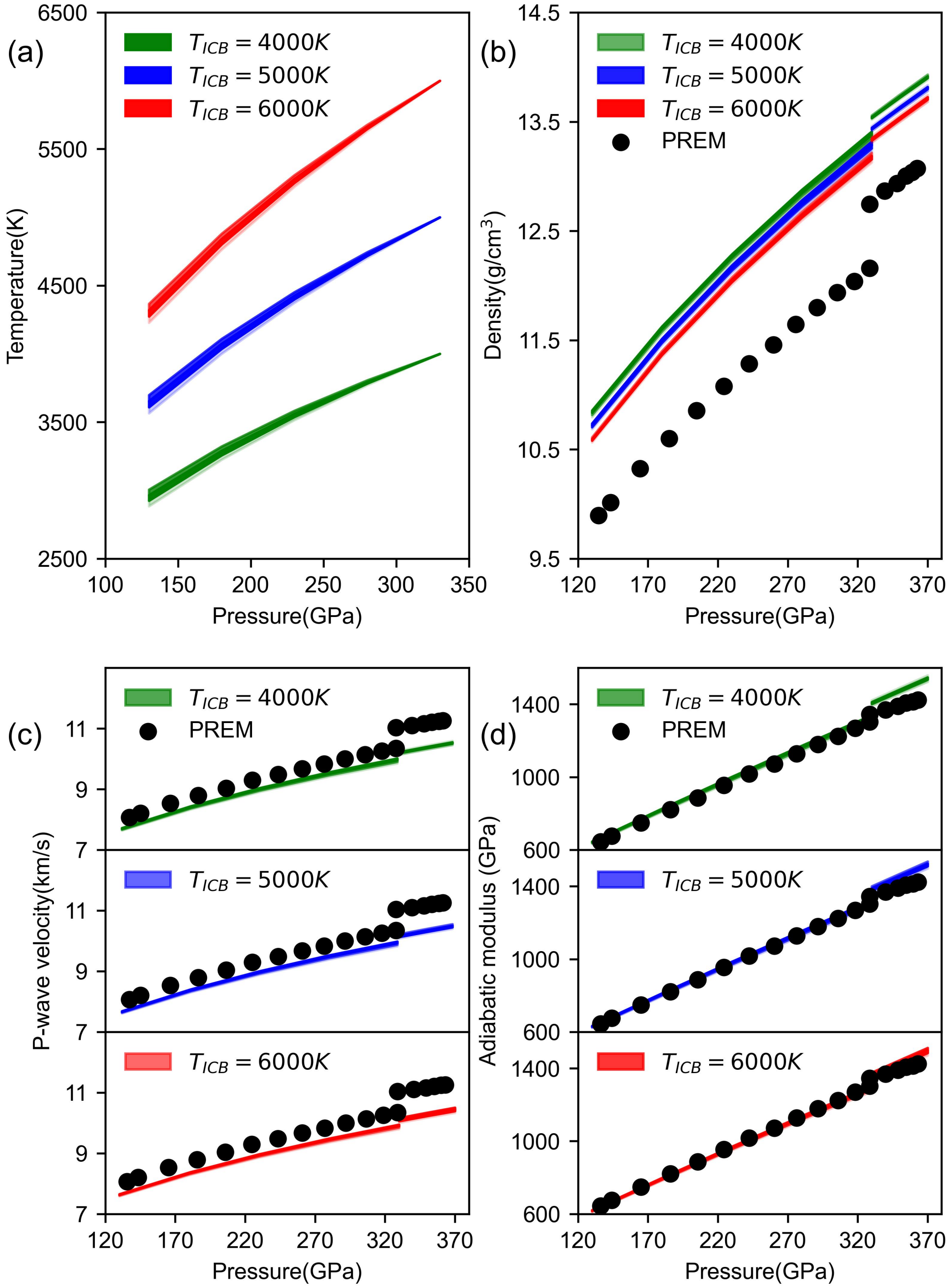

Figure 5. A comparison of the physical properties of liquid iron and hcp-iron, calculated based on an isentropic temperature profile, is conducted in conjunction with the PREM (Dziewoński & Anderson, 1981) data. Calculated isentropic temperature profile (a). Calculated density along the T_{ICB} isentrope (b). Calculated P-wave velocity along the isentrope (c). Calculated adiabatic bulk modulus along adiabats for solid and liquid iron (d). (When T_{ICB} takes the values of 4000 K, 5000 K, and 6000 K respectively)

The latent heat of fusion ($\Delta\ H_m$) released during the solidification of iron at the Earth's Inner Core Boundary plays a critical role in driving external convection in the core, contributing approximately 20% to the total energy. Based on the newly calculated latent heat of fusion for iron under ICB conditions-(0.526-0.973 kJ/g) -we re-evaluated the total energy released during Earth's core cooling process and its corresponding power output. Multiplying this latent heat by the mass of the core, estimated to be around 1.1 $\times 10^{23}$ kg, results in a total energy release of 8.987 $\times 10^{2}$ joules. Considering the shortest (0.565 billion years) and longest (4 billion years) estimates for the age of the core, and converting these durations into seconds, we further derived the power output range across these timescales: at the shortest time scale, the power output is approximately 3.244-6.002 TW, while at the longest time scale, it reduces to about 0.458-0.848 TW. This lower bound of the power output is essentially consistent with the results obtained by Singh (Singh et al., 2023b). These calculations provide a rough yet significant estimate, indicating that even over vast geological timescales, the Earth's core cooling process continuously releases enormous amounts of energy, which significantly sustains the operation of the geodynamo.

5 Conclusions

In this paper, we perform uncertainty quantization for parameters up to 40 dimensions in the multiphase iron equation of state based on Bayesian theory and MCMC sampling. When handling phase boundary data, we employ probability estimates derived from indirect measurements in lieu of direct measurement-based probability computations, allowing us to obtain the functional relationship between pressure and temperature without resorting to numerical inversion, significantly enhancing computational efficiency. The uncertainty quantization results of the parameters in the iron multiphase equation of state can not only reproduce the pressure, thermal fusion, modulus and expansion coefficient well, but also reproduce the phase diagram information and impact temperature data well. Under the assumption of an Inner Core Boundary (ICB) temperature of 5000 K, we have computed the range of density variation of liquid iron in the outer core region to be between 8.7% to 9.7%. This precise density differential data effectively constrains the estimation of possible light element content within the outer core. Furthermore, we have also reassessed the contribution to geomagnetic dynamo output power resulting from latent heat release during Earth's inner core cooling and solidification process, estimating this figure to fall within the interval of 0.458 to 6.002 TW. This body of research findings holds significant implications for advancing our understanding of the evolutionary history of the Earth's core.

Open Research Section

Data used in this study are available through the following sources:(Li et al., 2020; Morard et al., n.d.; O. L. Anderson, 1986; Kaufman et al., 1963; Johnson et al., 1962; Zhang & Guyot, 1999; Dewaele et al., 2015; Dewaele & Garbarino, 2017; Liu et al., 2013; Shibazaki et al., 2016; Nishihara et al., 2012; Shibazaki et al., 2020; Funamori et al., 1996; Anzellini et al., 2013; Komabayashi & Fei, 2010; Ohtani et al., 2013; Shahar et al., 2016; Sakai et al., 2014; Komabayashi et al., 2009; Yamazaki et al., 2012; González-Cataldo & Militzer, 2023; Kuwayama et al., 2020; Brown & Mcqueen, 1986; Brown et al., 2000; W. W. Anderson & Ahrens, 1994; Desai, 1986)

Acknowledgments

This work was supported by the National Key R&D Program of China (Grant No. 2021YFB3802300), the National Nature Science Foundation of China (Grant Nos. 12372370).

References

Alfè, D., Price, G. D., & Gillan, M. J. (2002, Apr). Iron under earth's core conditions: Liquid-state thermodynamics and high-pressure melting curve from ab initio calculations. *Phys. Rev. B*, *65*, 165118. Retrieved from `https://link.aps.org/doi/10.1103/PhysRevB.65.165118` doi: 10.1103/PhysRevB.65.165118

Anderson, O. L. (1986). Properties of iron at the earth's core conditions. *Geophysical Journal International*, *84*, 561-579. Retrieved from `https://api.semanticscholar.org/CorpusID:128695991`

Anderson, W. W., & Ahrens, T. (1994). An equation of state for liquid iron and implications for the earth's core. *Journal of Geophysical Research*, *99*, 4273-4284. Retrieved from `https://api.semanticscholar.org/CorpusID:27551780`

Anzellini, S., Dewaele, A., Mezouar, M., Loubeyre, P., & Morard, G. (2013). Melting of iron at earth's inner core boundary based on fast x-ray diffraction. *Science*, *340*, 464 - 466. Retrieved from `https://api.semanticscholar.org/CorpusID:31604508`

Brown, J. M., Fritz, J. N., & Hixson, R. S. (2000). Hugoniot data for iron. *Journal of Applied Physics*, *88*, 5496-5498. Retrieved from `https://api.semanticscholar.org/CorpusID:121588362`

Brown, J. M., & Mcqueen, R. G. (1986). Phase transitions, grüneisen parameter, and elasticity for shocked iron between 77 gpa and 400 gpa. *Journal of Geophysical Research*, *91*, 7485-7494. Retrieved from `https://api.semanticscholar.org/CorpusID:129107803`

Desai, P. D. (1986). Thermodynamic properties of iron and silicon. *Journal of Physical and Chemical Reference Data*, *15*, 967-983. Retrieved from `https://api.semanticscholar.org/CorpusID:95590422`

Dewaele, A., Denoual, C., Anzellini, S., Occelli, F., Mezouar, M., Cordier, P., … Rausch, E. (2015, May). Mechanism of the $\alpha - \epsilon$ phase transformation in iron. *Phys. Rev. B*, *91*, 174105. Retrieved from `https://link.aps.org/doi/10.1103/PhysRevB.91.174105` doi: 10.1103/PhysRevB.91.174105

Dewaele, A., & Garbarino, G. (2017). Low temperature equation of state of iron. *Applied Physics Letters*, *111*, 021903. Retrieved from `https://api.semanticscholar.org/CorpusID:103212786`

Dorogokupets, P. I. e. a. (2017). Thermodynamics and equations of state of iron to 350 gpa and 6000 k. *Scientific Reports*, *7*, 41863. doi: 10.1038/srep41863

Dziewoński, A. M., & Anderson, D. L. (1981). Preliminary reference earth model. *Physics of the Earth and Planetary Interiors*, *25*, 297-356. Retrieved from `https://api.semanticscholar.org/CorpusID:129232713`

Fei, Y., Murphy, C. A., Shibazaki, Y., Shahar, A., & Huang, H. (2016). Thermal equation of state of hcp-iron: Constraint on the density deficit of earth's solid inner core. *Geophysical Research Letters*, *43*, 6837 - 6843. Retrieved from `https://api.semanticscholar.org/CorpusID:132866914`

Foreman-Mackey, D., Hogg, D. W., Lang, D., & Goodman, J. (2013, March). emcee: The MCMC Hammer. , *125*(925), 306. doi: 10.1086/670067

Funamori, N., Yagi, T., & Uchida, T. (1996). High-pressure and high-temperature in situ x-ray diffraction study of iron to above 30 gpa using ma8-type apparatus. *Geophysical Research Letters*, *23*, 953-956. Retrieved from `https://api.semanticscholar.org/CorpusID:128619359`

González-Cataldo, F., & Militzer, B. (2023). Ab initio determination of iron melting at terapascal pressures and super-earths core crystallization. *Physical Review Research*. Retrieved from `https://api.semanticscholar.org/CorpusID:262178924`

Harris, C. R., Millman, K. J., van der Walt, S. J., Gommers, R., Virtanen, P., Cournapeau, D., … Oliphant, T. E. (2020, September). Array programming with

NumPy. *Nature*, *585*(7825), 357–362. Retrieved from https://doi.org/10.1038/s41586-020-2649-2 doi: 10.1038/s41586-020-2649-2

Hirose, K., Wood, B. J., & Voadlo, L. (2021). Light elements in the earth's core. *Nature Reviews Earth & Environment*, *2*, 645 - 658. Retrieved from https://api.semanticscholar.org/CorpusID:237272150

Ichikawa, H., Tsuchiya, T., & Tange, Y. (2014). The p-v-t equation of state and thermodynamic properties of liquid iron. *Journal of Geophysical Research: Solid Earth*, *119*, 240 - 252. Retrieved from https://api.semanticscholar.org/CorpusID:130604173

Johnson, P. C., Stein, B. A., & Davis, R. S. (1962). Temperature dependence of shock-induced phase transformations in iron. *Journal of Applied Physics*, *33*, 557-561. Retrieved from https://api.semanticscholar.org/CorpusID:120137987

Kaufman, L., Clougherty, E. V., & Weiss, R. J. (1963). The lattice stability of metals*iii*. iron. *Acta Metallurgica*, *11*, 323-335. Retrieved from https://api.semanticscholar.org/CorpusID:94888216

Komabayashi, T., & Fei, Y. (2010). Internally consistent thermodynamic database for iron to the earth's core conditions. *Journal of Geophysical Research*, *115*, 1-12. Retrieved from https://api.semanticscholar.org/CorpusID:54919859

Komabayashi, T., Fei, Y., Meng, Y., & Prakapenka, V. B. (2009). In-situ x-ray diffraction measurements of the γ-ϵ transition boundary of iron in an internally-heated diamond anvil cell. *Earth and Planetary Science Letters*, *282*, 252-257. Retrieved from https://api.semanticscholar.org/CorpusID:130768562

Kuwayama, Y., Morard, G., Nakajima, Y., Hirose, K., Baron, A. Q., Kawaguchi, S. I., … Ohishi, Y. (2020). Equation of state of liquid iron under extreme conditions. *Physical review letters*, *124 16*, 165701. Retrieved from https://api.semanticscholar.org/CorpusID:218562532

Labrosse, S. (2014). Thermal evolution of the core with a high thermal conductivity. *Physics of the Earth and Planetary Interiors*, *247*, 36-55. Retrieved from https://api.semanticscholar.org/CorpusID:122507563

Li, J., & Fei, Y. (2014). Experimental constraints on core composition.. Retrieved from https://api.semanticscholar.org/CorpusID:92064071

Li, J., Wu, Q., Li, J., Xue, T., Tan, Y., Zhou, X., … Sekine, T. (2020). Shock melting curve of iron: A consensus on the temperature at the earth's inner core boundary. *Geophysical Research Letters*, *47*. Retrieved from https://api.semanticscholar.org/CorpusID:225363462

Lindquist, B. A., & Jadrich, R. B. (2022). Uncertainty quantification for a multiphase carbon equation of state model. *Journal of Applied Physics*. Retrieved from https://api.semanticscholar.org/CorpusID:248331170

Liu, J., Lin, J., Alatas, A., & Bi, W. (2013). Sound velocities of bcc-fe and fe0.85si0.15 alloy at high pressure and temperature. *Physics of the Earth and Planetary Interiors*, *233*, 24-32. Retrieved from https://api.semanticscholar.org/CorpusID:21680558

Morard, G., Boccato, S., Rosa, A. D., Anzellini, S., Miozzi, F., Henry, L., … Torchio, R. (n.d.). Solving controversies on the iron phase diagram under high pressure. *Geophysical Research Letters*, *45*, 11,074 - 11,082. Retrieved from https://api.semanticscholar.org/CorpusID:92985762

Murphy, C. A., Jackson, J. M., & Sturhahn, W. (2013). Experimental constraints on the thermodynamics and sound velocities of hcp-fe to core pressures. *Journal of Geophysical Research: Solid Earth*, *118*, 1999 - 2016. Retrieved from https://api.semanticscholar.org/CorpusID:28881426

Nishihara, Y., Nakajima, Y., Akashi, A., Tsujino, N., Takahashi, E., Funakoshi, K., & Higo, Y. (2012). Isothermal compression of face-centered cubic iron. *American Mineralogist*, *97*, 1417 - 1420. Retrieved from `https://api.semanticscholar.org/CorpusID:54601004`

Ohtani, E., Shibazaki, Y., Sakai, T., Mibe, K., Fukui, H., Kamada, S., … Baron, A. Q. (2013). Sound velocity of hexagonal close-packed iron up to core pressures. *Geophysical Research Letters*, *40*, 5089 - 5094. Retrieved from `https://api.semanticscholar.org/CorpusID:128586157`

Sakai, T., Takahashi, S., Nishitani, N., Mashino, I., Ohtani, E., & Hirao, N. (2014). Equation of state of pure iron and fe0.9ni0.1 alloy up to 3mbar. *Physics of the Earth and Planetary Interiors*, *228*, 114-126. Retrieved from `https://api.semanticscholar.org/CorpusID:129344647`

Shahar, Anat, Murphy, Caitlin, Fei, Yingwei, … Yuki (2016). Thermal equation of state of hcp-iron: Constraint on the density deficit of earth's solid inner core. *Geophysical Research Letters*, *43*(13), 6837-6843.

Shibazaki, Y., Nishida, K., Higo, Y., Igarashi, M., Tahara, M., Sakamaki, T., … Ohtani, E. (2016). Compressional and shear wave velocities for polycrystalline bcc-fe up to 6.3 gpa and 800 k. *American Mineralogist*, *101*, 1150 - 1160. Retrieved from `https://api.semanticscholar.org/CorpusID:101475614`

Shibazaki, Y., Nishida, K., Tobe, H., Terasaki, H., & Higo, Y. (2020). Effect of hydrogen on the sound velocity of fcc-fe at high pressures and high temperatures.. Retrieved from `https://api.semanticscholar.org/CorpusID:222954715`

Singh, S., Briggs, R., Gorman, M. G., Benedict, L. X., Wu, C. J., Hamel, S., … Smith, R. F. (2023a). A structural study of hcp and liquid iron under shock compression up to 275 gpa.. Retrieved from `https://api.semanticscholar.org/CorpusID:258180169`

Singh, S., Briggs, R., Gorman, M. G., Benedict, L. X., Wu, C. J., Hamel, S., … Smith, R. F. (2023b). Structural study of hcp and liquid iron under shock compression up to 275 gpa. *Physical Review B*. Retrieved from `https://api.semanticscholar.org/CorpusID:265190891`

Sinmyo, R., Hirose, K., & Ohishi, Y. (2018). Melting curve of iron to 290 gpa determined in a resistance-heated diamond-anvil cell. *Earth and Planetary Science Letters*. Retrieved from `https://api.semanticscholar.org/CorpusID:134890949`

Stacey, F. D., & Davis, P. (2004). High pressure equations of state with applications to the lower mantle and core. *Physics of the Earth and Planetary Interiors*, *142*, 137-184. Retrieved from `https://api.semanticscholar.org/CorpusID:129634838`

Tateno, S., Hirose, K., Ohishi, Y., & Tatsumi, Y. (2010). The structure of iron in earth's inner core. *Science*, *330*, 359 - 361. Retrieved from `https://api.semanticscholar.org/CorpusID:206528628`

Waskom, M. L. (2021). seaborn: statistical data visualization. *Journal of Open Source Software*, *6*(60), 3021. Retrieved from `https://doi.org/10.21105/joss.03021` doi: 10.21105/joss.03021

Yamazaki, D., Ito, E., Yoshino, T., Yoneda, A., Guo, X., Zhang, B., … Funakoshi, K. (2012). P-v-t equation of state for ϵ-iron up to 80 gpa and 1900 k using the kawai-type high pressure apparatus equipped with sintered diamond anvils. *Geophysical Research Letters*, *39*. Retrieved from `https://api.semanticscholar.org/CorpusID:129695765`

Zhang, J., & Guyot, F. (1999). Thermal equation of state of iron and fe0.91si0.09. *Physics and Chemistry of Minerals*, *26*, 206-211. Retrieved from `https://api.semanticscholar.org/CorpusID:97322900`

Obtaining the Equation of State for Multiphase Iron under Earth's Core Conditions using Bayesian Statistics

Run Wu[1], Shikai Xiang[2*], Yi Sun[2*], Yunting Xian[3], Yin Luo[4], Feifan Dai[5]

National Key Laboratory of Shock Wave and Detonation Physics, Institute of Fluid Physics
China Academy of Engineering Physics, Mianyang 621999, China

Key Points:

- Under the framework of Bayesian statistics, the uncertainty of parameters in the multiphase equation of state of iron is quantified.
- A simple and accurate probability method for calculating the phase boundary data of iron is proposed
- EOS estimates Earth's outer core density deficit at 8.7%-9.7% and geomagnetic power output from inner core cooling at 0.458-6.002 TW.

Plain Language Summary

Iron constitutes the primary element of the Earth's core, and understanding its thermodynamic properties is essential. The equation of state for iron is crucial for these insights. However, the inherent uncertainties in experimental data can significantly impact the parameters that define iron's equation of state. To address this, we employed Bayesian statistics coupled with Markov chain Monte Carlo (MCMC) simulations, allowing us to quantify the uncertainties surrounding these parameters. In our approach, we developed a straightforward yet effective method to calculate the probability associated with phase boundary data during the simulation process. The outcomes from our simulations yielded an equation of state that precisely mirrored a variety of experimental data sets, including phase boundary measurements, static pressure readings under diverse conditions, shock wave observations, and acoustic velocity determinations across different states. Armed with 100 posterior parameter samples, we honed in on the Earth's outer core density deficit, predicting it to fall within a range of approximately 8.7% to 9.7%. Furthermore, we estimated the geodynamo power output, generated by the latent heat released during the cooling and solidification of the Earth's inner core, to be between 0.458 and 6.002 terawatts.

Corresponding author: Shikai Xiang, `skxiang@caep.cn`

Corresponding author: Yi Sun, `ssunyyi@163.com`

Abstract

Iron is the primary constituent element of Earth's core, and its equation of state plays a pivotal role in understanding the thermodynamic properties of the core. However, uncertainties in experimental data have significant effects on the parameters within the iron equation of state. Using Bayesian statistical analysis coupled with Markov chain Monte Carlo (MCMC) simulation methods, we quantified the uncertainties in the equation of state parameters. During the simulation process, we proposed a simple yet efficient computational method for determining the probability of phase boundary data. The equation of state we obtained accurately reproduces various experimental data, including phase boundary experiments, static pressure data under different conditions, shock wave data, and sound velocity data at different states. With 100 posterior parameter samples, we predict that the density deficit of Earth's outer core falls within a range of approximately 8.7% to 9.7%, and the geodynamo power output due to latent heat release during the cooling and solidification of Earth's inner core is estimated to be between 0.458 to 6.002 terawatts.

1 Introduction

The Earth's core is primarily composed of iron, with minor inclusions of lighter elements such as nickel, sulfur, and oxygen (Li & Fei, 2014; Hirose et al., 2021). Iron significantly influences the propagation of seismic waves, and by meticulously analyzing these waves in conjunction with the equation of state for iron, we can deduce the spatial distribution of iron and other light elements within the core (Dziewoński & Anderson, 1981; Ichikawa et al., 2014; Kuwayama et al., 2020), thus revealing its complex structure. Additionally, the formation of the Earth's magnetic field is linked to the flow in the electrically conductive liquid outer core, a process driven by thermal convection (Labrosse, 2014; Singh et al., 2023a). Therefore, an in-depth study of the physical properties of iron under core conditions is of irreplaceable importance for elucidating the generation mechanism and evolutionary history of the Earth's magnetic field. Overall, investigating the thermodynamic behavior of iron under extreme high pressure is crucial for addressing fundamental questions about the Earth's core structure and dynamics; the precise equation of state for iron is key to these research topics.

Traditional methods for determining parameters in the equation of state model may introduce inaccuracies due to data uncertainty. Recognizing this is particularly important when studying the role of iron in the Earth's core. Although past studies have explored the equation of state for iron experimentally, they often did not utilize Bayesian data analysis, which incorporates prior knowledge and data uncertainty. Bayesian methods provide a probability distribution of parameters, continually updating it with new data, thus enhancing simulation accuracy and deepening our understanding of Earth's interior processes. In the Bayesian framework, conventional approaches determine phase transition boundaries based on Gibbs free energy but require complex numerical computations. To simplify this, Lindquist and Jadrich (Lindquist & Jadrich, 2022) introduced a model that categorized phase diagram data effectively. We focus on solving the phase boundary problem quickly and accurately, avoiding numerical inversion while adhering to the principle of equal Gibbs free energy between phases, significantly improving efficiency and accurately reproducing phase boundaries.

2 Simulation Methodology and Details

In data analysis, Bayesian statistics and Markov chain Monte Carlo (MCMC) methods are closely coupled to effectively manage uncertainty. Bayesian inference combines prior knowledge with new data to generate probabilistic distributions of model parameters, offering a more holistic perspective on uncertainty than traditional methods. In the study of multiphase equations, leveraging phase boundary data to constrain model parameters is an efficient approach, typically involving measurements of pressure (P) and temperature (T). Conventional methods are based on the principle of Gibbs free energy equilibrium and require numerical inversion to determine the relationship between P and T (P(T) or T(P)) for subsequent MCMC calculations of system state probabilities. However, this computational process is costly when dealing with complex inverse relationships between P and T. To enhance efficiency, Lindquist and Jadrich (Lindquist & Jadrich, 2022) innovatively transformed phase diagram data into a probability classification problem in their study of carbon's equation of state, achieving notable success. We also propose a simplified method that avoids complex numerical inversion while maintaining equal Gibbs free energy at phase boundaries. Specifically, we use probability estimates derived from indirect measurements to handle phase boundaries, rather than direct measurement-based probability computations, thus obtaining the P-T relationship without the need for numerical inversion, significantly improving computational efficiency. The details of our innovative phase boundary handling technique and parameter quantification can be found in the supplementary materials Text S2 and Text S3.

3 Multi-phase state equation of iron

In this study, we utilized the Python-emcee library (Foreman-Mackey et al., 2013) for parameter sampling, coupled with Python-numpy (Harris et al., 2020) for efficient data manipulation, and leveraged Python-seaborn (Waskom, 2021) to create visualizations, thereby facilitating in-depth analysis and intuitive representation of the data. Employing Bayesian theory and MCMC sampling techniques, we obtained a set of samples for the 40-dimensional parameters within the model (Dorogokupets, 2017). Through marginalization, we derived the marginal posterior distributions for each parameter, presenting them graphically to illustrate individual parameter behavior. Additionally, we computed and plotted a correlation matrix to visually depict inter-parameter relationships. Furthermore, based on 1000 sets of sample parameters, we estimated the parameter values corresponding to the maximum posterior probability (MPP). Detailed results can be found in the supplementary information Text S4.

The Fig.1 shows the phase diagram obtained using Maximum Posterior Probability (MPP) for parameter estimation. Along the isotherm at 300K, we calculate the bcc-hcp phase transition pressure to be 16.9 GPa. At a pressure of 0.1 MPa, the transformation temperatures from bcc(a) to fcc and from bcc(delta) to fcc are calculated to be 1190 K and 1611 K, respectively, with the melting point reaching 1801 K. We further computed the triple points where the bcc-fcc-liquid triple point is located at 6.0 GPa and 1994 K, the bcc-fcc-hcp triple point at 11.6 GPa and 774 K, and the fcc-hcp-liquid triple point at 109.5 GPa and 3698 K. Near the fcc-hcp-liquid triple point, our calculated phase boundary lines agree with the experimental data of Anzellini et al (Anzellini et al., 2013) and Morard et al (Morard et al., n.d.), but there is a discrepancy with the data of Sinmyo et al (Sinmyo et al., 2018). This mismatch may arise because our simulation dataset only included Morard's experimental data. In the high-pressure region, our calculated melting line for the hcp phase aligns with data based on ab initio free energy calculations (Alfè et al., 2002) and experimental data obtained by Li et al (Li et al., 2020). Additionally, the figure depicts the shock Hugoniot within the hcp phase, plotted using 100 sets of parameters, represented by thick black lines. The calculated shock curve intersects the melting line at the shock-induced melting point, which is located at 215 GPa and 5100 K. (The relationship between the shock wave and particle velocity used here is based on research by Brown (Brown et al., 2000).) .From the overall results, our calculated outcomes can accurately reproduce the phase boundary data and the shock Hugoniot within the hcp phase.

The Fig.2 displays the deviations between the pressure values calculated using MPP parameters for the various phases of iron (bcc, fcc, hcp, liquid) and the reference datasets.

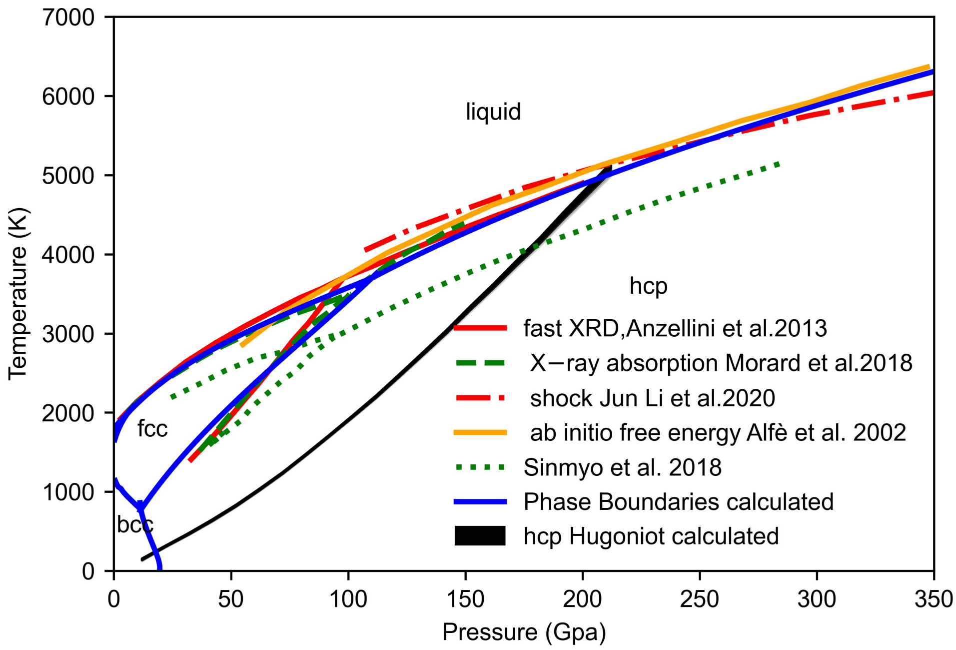

Figure 1. The figure presents a comparison of the calculated phase boundaries for iron obtained using maximum a posteriori parameter estimates against the reference boundary data(Anzellini et al., 2013; Morard et al., n.d.; Li et al., 2020; Alfè et al., 2002; Sinmyo et al., 2018). The black shaded area represents the shock curves within the hcp phase, computed using 100 sets of parameters; the relationship between the shock wave and particle velocity employed here is sourced from Brown (Brown et al., 2000).

.

For the Fe-bcc phase, based on experimental data (Zhang & Guyot, 1999; Dewaele et al., 2015; Dewaele & Garbarino, 2017; Liu et al., 2013; Shibazaki et al., 2016), the maximum deviation of our calculated results is less than 2 GPa. In the Fe-fcc phase, the maximum discrepancy between our computed pressure data and the experimental pressure data does not exceed 5 GPa (Nishihara et al., 2012; Shibazaki et al., 2020; Funamori et al., 1996; Anzellini et al., 2013; Komabayashi & Fei, 2010). Regarding the Fe-hcp phase, except for one set of anomalous data points (Tateno et al., 2010), the deviations of other data (Ohtani et al., 2013; Shahar et al., 2016; Sakai et al., 2014; Komabayashi et al., 2009; Yamazaki et al., 2012; Anzellini et al., 2013; González-Cataldo & Militzer, 2023) from our calculations are mostly within 10 GPa. However, some experimental data for the liquid phase (Kuwayama et al., 2020) show significant differences with the calculated results, which is likely due to substantial experimental errors. These experimental data were measured at multiple temperatures, not under isothermal conditions, and due to the density of the data, it is difficult to clearly label each temperature point on the graph.

The Fig.3 presents a comparison between the calculated shock-experiment-based pressures and the actual experimental measurements. Our calculations indicate that the onset of the shock melting curve for hcp iron occurs at a pressure of 215 GPa. However, the majority of empirical evidence suggests that the actual shock melting pressure is around 220 GPa. Therefore, Fig.3(a) focuses on the shock pressure range below 220 GPa, illustrating the deviation between the calculated shock pressure data and the experimentally determined pressure values within this range. As can be seen from the figure, these deviations are kept within 5 GPa, demonstrating a high degree of consistency between the our calculated results and experimental observations.To further understand the behavior of iron under extreme conditions, particularly in the fully molten state, Fig.3(b) provides a detailed comparison between computational and experimental data within the dynamic high-pressure range of 260 to 480 GPa. In this higher pressure interval, most of the data deviations are still maintained below 10 GPa, indicating that even under very high dynamic pressures, our computational data maintains good agreement with the experimental data (Brown & Mcqueen, 1986; Brown et al., 2000; W. W. Anderson & Ahrens, 1994; Li et al., 2020), thereby validating the accuracy and reliability of our computational results. Synthesizing these findings, our equations of state obtained through MPP parameter estimations are capable of effectively replicating the pressure characteristics of iron across a considerable range.

The Fig.4(a) demonstrates that at room temperature conditions (300 K), the calculated bulk wave speeds in the hexagonal close-packed (hcp) structure across various pressures (30-170 GPa) are higher relative to Murphy's experimental data (Murphy et al., 2013), yet within this pressure range, we also identified that Ohtani's longitudinal wave speed experimental data (Ohtani et al., 2013) are consistently higher than Murphet's measurements. Fig.4(b) shows that within this temperature range, our computed sound velocity data exhibit good agreement with Kuwayama's experimental results (Kuwayama et al., 2020) from High-pressure inelastic x-ray scattering (IXS) measurements of liquid iron. Moreover, when comparing our shock-induced high-pressure acoustic speeds to the findings of Anderson's research (W. W. Anderson & Ahrens, 1994), our calculations reveal a maximum deviation of less than 6.6%, thus confirming the consistency and accuracy of our work.

Furthermore, in the supplementary material Text S5 section, this study compares a series of experimental measurements of physical properties with the results calculated from 100 parameter samples derived from posterior distribution sampling. Our computational findings indicate that the heat capacity of the body-centered cubic (bcc) structure is largely consistent with the experimental data reported by Desai (Desai, 1986). However, at the Curie temperature of 1043 K, the experimentally measured heat capacity significantly exceeds our computational results, which may be attributed to an insufficient model description of the ferromagnetic transition process. Regarding the ther-

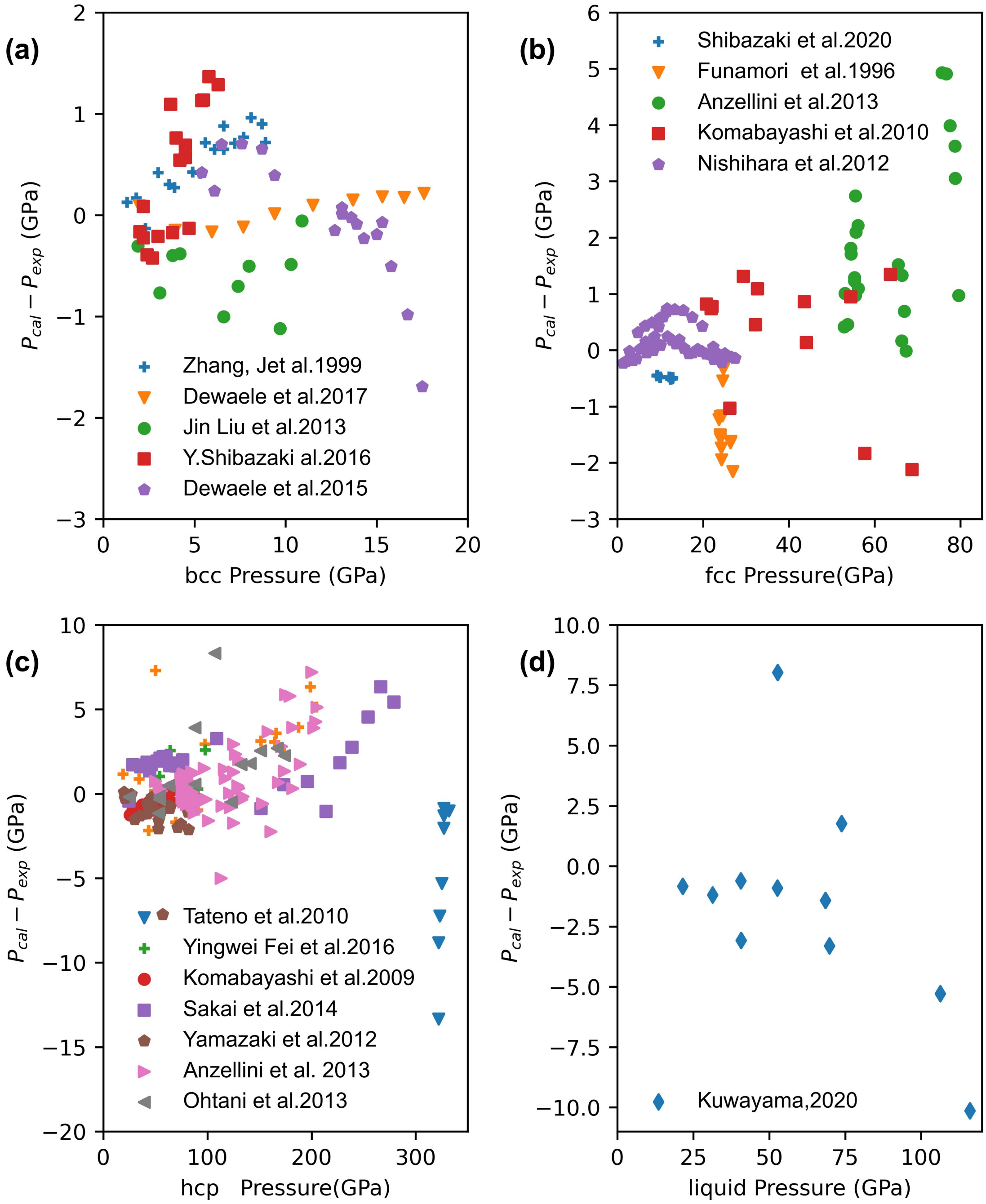

Figure 2. The Fig.2 illustrates the discrepancies between the pressure values computed utilizing MPP parameters applied to various phases of Iron - bcc (a), fcc (b), hcp (c), Liquid (d) - and corresponding reference static high pressure data sets.

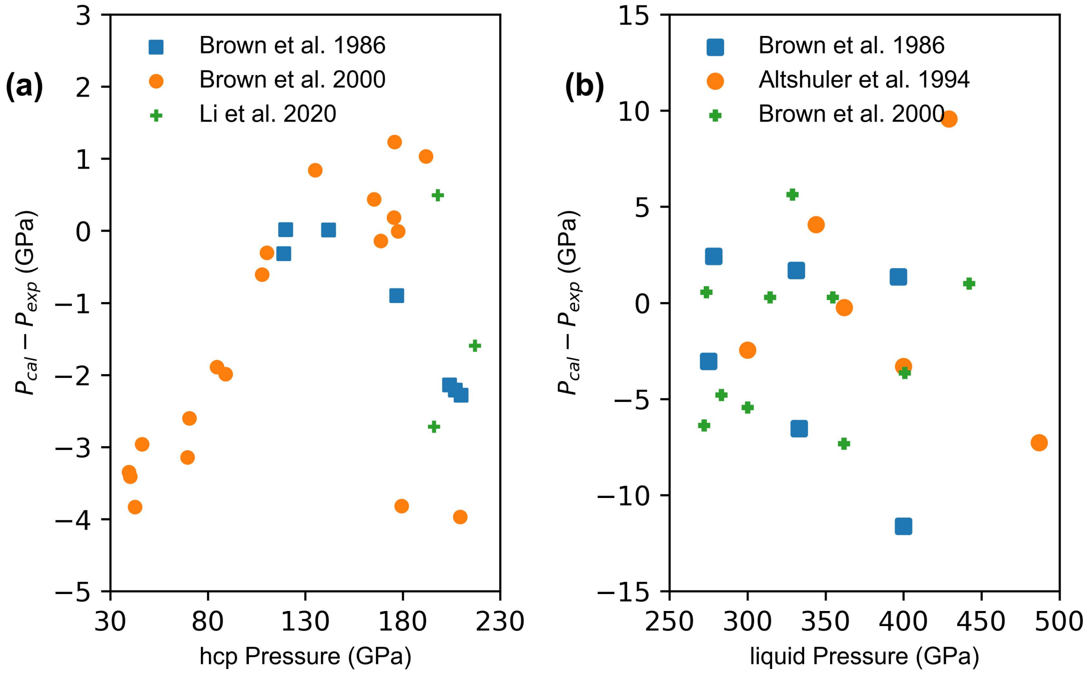

Figure 3. The picture we use MPP parameters estimation to calculate the differences between the computed dynamic high-pressure data for the hcp phase and the liquid phase, and compare them with the corresponding shock experimental data (Brown & Mcqueen, 1986; Brown et al., 2000; W. W. Anderson & Ahrens, 1994; Li et al., 2020).

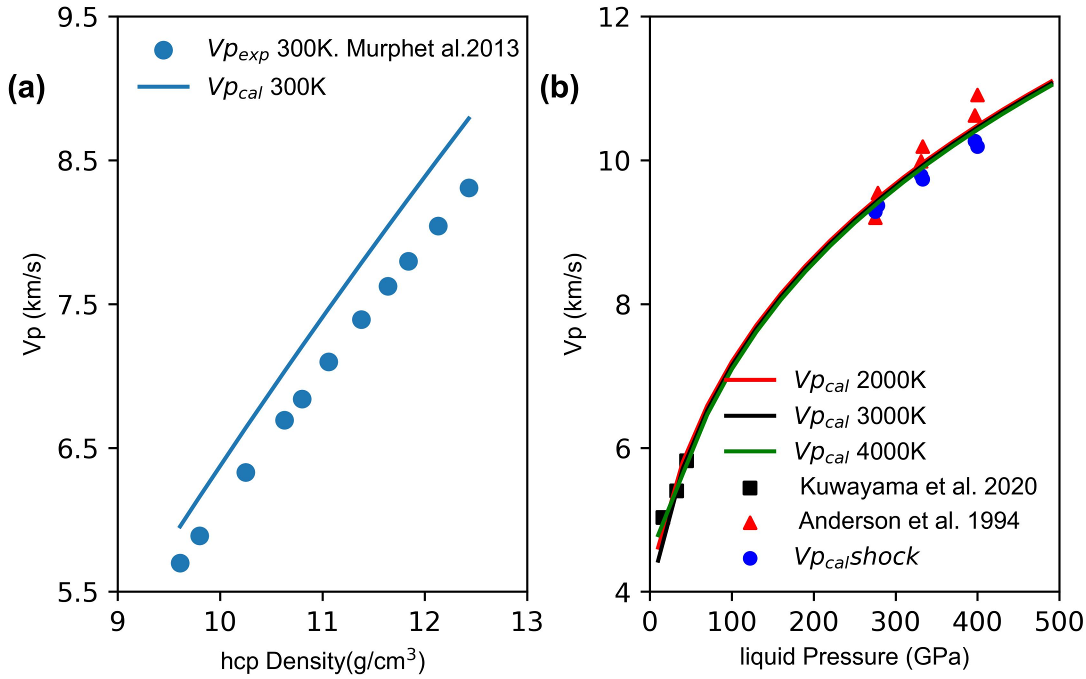

Figure 4. In figure (a), the blue solid line indicates the bulk sound speed of hcp-iron at 300K as calculated by us, and the corresponding blue dots represent experimental data from Murphy (Murphy et al., 2013).In the figure (b), solid lines show our calculated sound speeds at 2000K, 3000K, and 4000K. Black squares are IXS experimental data (Kuwayama et al., 2020); red triangles, shock experiment data (W. W. Anderson & Ahrens, 1994); and blue circles, corresponding shock calculation results.

mal expansion coefficient of iron in bcc and face-centered cubic (fcc) structures, our calculations are in agreement with the experimental data from Dorogokupets's supplementary materials (Dorogokupets, 2017) at lower temperatures; however, at higher temperatures, the computed values are slightly below the experimental observations, possibly due to inadequate experimental constraints applied during the simulation phase. Concerning the isothermal pressure curves of solid phases, our computational results demonstrate that the pressure curves for bcc-Fe at 15 K and 300 K, as well as fcc-Fe at 1073 K and 1273 K, and hcp-Fe at various temperatures, closely match the experimental data (Dewaele & Garbarino, 2017; Liu et al., 2013; Nishihara et al., 2012; Fei et al., 2016). Similar to the heat capacity calculations, the uncertainty range of the isothermal pressure curves is relatively small.

Overall, by utilizing Bayesian statistical theory and MCMC sampling methods, we have systematically obtained the uncertainties of the parameters in iron's equation of state. The simulation results effectively model the diverse behaviors of iron under various conditions of pressure, volume, and temperature, including heat fusion and thermal expansion at ambient pressure as temperatures change, pressure variations at different temperatures, and performance during shock experiments and phase boundary transitions. We achieved equation of state predictions for pressures that cover the range of the Earth's core, with subsequent presentation of our predictions for the thermodynamic properties of the Earth's core to follow.

4 Applications under the Earth core conditions

To accurately quantify certain thermodynamic properties of the Earth's core, we selected 100 sets of sample parameters to assess the uncertainty range in predicted physical quantities introduced by calibration data errors through simulation calculations.

In the simulation study, we have conducted calculations on the melting characteristics of pure iron under conditions at the Earth's Inner Core Boundary (ICB), where at a pressure of 330 GPa, the theoretical melting temperature range for pure iron is between 5997 K and 6262 K. However, the actual melting temperature in the core might be lower due to the presence of lighter elements. To validate these computational results against geological experimental data, we plotted the density(ρ), sonic velocity(V_P), and shear modulus(K_S) of liquid pure iron at various temperatures (4000 K, 5000 K, and 6000 K) under ICB pressure, comparing them with data from the Preliminary Reference Earth Model (PREM) (Dziewoński & Anderson, 1981). The relevant details are shown in the Fig.5. The solid-liquid phase transition temperatures (at the CMB) computed by us spanned intervals of (2928 K-3086 K), (3621 K-3795 K), and (4297 K-4479 K). When setting T_{ICB} at 5000 K, this upper limit approximates the 3800 K proposed by Brown and McQueen in 1986 (Brown & Mcqueen, 1986), as well as the 3739 K given by Stacey and Davis in 2004 (Stacey & Davis, 2004). Adopting a value of 4676 K yields a CMB temperature range of (3398 K-3568 K), which aligns closely with Anderson's 3637 K and Ichikawa's 3585 K (Ichikawa et al., 2014).

Assuming T_{ICB} to be 5000 K, the estimated densities of liquid iron at the CMB and ICB conditions are respectively (10.854 g/cm^3- 10.786 g/cm^3) and (13.226 g/cm^3 - 13.348 g/cm^3). Moreover, the graphs reveal that both the sonic velocity and shear modulus exhibit relatively low sensitivity to temperature changes; our computations show that the outer core's values in these two physical parameters are nearly consistent with PREM data, with small discrepancies in sonic velocity. The figures also demonstrate that the difference in density between solid and liquid iron $\Delta\rho_{solid}$ at the ICB is less than the density change resulting from internal state variations within liquid iron $\Delta\rho_{liquid}$, suggesting compositional differences between the inner and outer cores. Nevertheless, the calculated density deviation range for the outer core (8.7% to 9.7%) provides a strong constraint on the content of light elements.

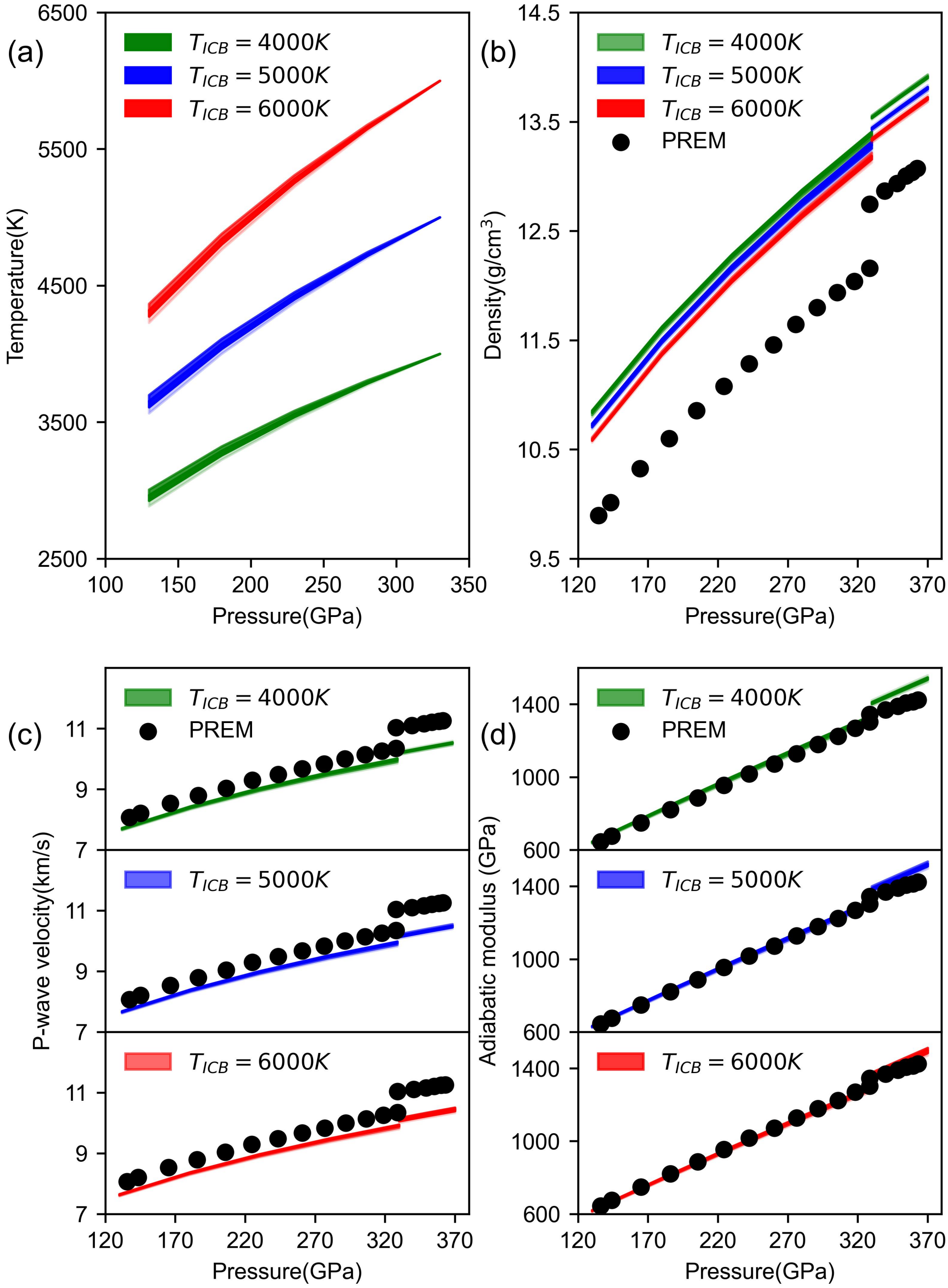

Figure 5. A comparison of the physical properties of liquid iron and hcp-iron, calculated based on an isentropic temperature profile, is conducted in conjunction with the PREM (Dziewoński & Anderson, 1981) data. Calculated isentropic temperature profile (a). Calculated density along the T_{ICB} isentrope (b). Calculated P-wave velocity along the isentrope (c). Calculated adiabatic bulk modulus along adiabats for solid and liquid iron (d). (When T_{ICB} takes the values of 4000 K, 5000 K, and 6000 K respectively)

The latent heat of fusion ($\Delta\ H_m$) released during the solidification of iron at the Earth's Inner Core Boundary plays a critical role in driving external convection in the core, contributing approximately 20% to the total energy. Based on the newly calculated latent heat of fusion for iron under ICB conditions-(0.526-0.973 kJ/g) -we re-evaluated the total energy released during Earth's core cooling process and its corresponding power output. Multiplying this latent heat by the mass of the core, estimated to be around 1.1 $\times\ 10^{23}$ kg, results in a total energy release of 8.987×10^{2} joules. Considering the shortest (0.565 billion years) and longest (4 billion years) estimates for the age of the core, and converting these durations into seconds, we further derived the power output range across these timescales: at the shortest time scale, the power output is approximately 3.244-6.002 TW, while at the longest time scale, it reduces to about 0.458-0.848 TW. This lower bound of the power output is essentially consistent with the results obtained by Singh (Singh et al., 2023b). These calculations provide a rough yet significant estimate, indicating that even over vast geological timescales, the Earth's core cooling process continuously releases enormous amounts of energy, which significantly sustains the operation of the geodynamo.

5 Conclusions

In this paper, we perform uncertainty quantization for parameters up to 40 dimensions in the multiphase iron equation of state based on Bayesian theory and MCMC sampling. When handling phase boundary data, we employ probability estimates derived from indirect measurements in lieu of direct measurement-based probability computations, allowing us to obtain the functional relationship between pressure and temperature without resorting to numerical inversion, significantly enhancing computational efficiency. The uncertainty quantization results of the parameters in the iron multiphase equation of state can not only reproduce the pressure, thermal fusion, modulus and expansion coefficient well, but also reproduce the phase diagram information and impact temperature data well. Under the assumption of an Inner Core Boundary (ICB) temperature of 5000 K, we have computed the range of density variation of liquid iron in the outer core region to be between 8.7% to 9.7%. This precise density differential data effectively constrains the estimation of possible light element content within the outer core. Furthermore, we have also reassessed the contribution to geomagnetic dynamo output power resulting from latent heat release during Earth's inner core cooling and solidification process, estimating this figure to fall within the interval of 0.458 to 6.002 TW. This body of research findings holds significant implications for advancing our understanding of the evolutionary history of the Earth's core.

Open Research Section

Data used in this study are available through the following sources:(Li et al., 2020; Morard et al., n.d.; O. L. Anderson, 1986; Kaufman et al., 1963; Johnson et al., 1962; Zhang & Guyot, 1999; Dewaele et al., 2015; Dewaele & Garbarino, 2017; Liu et al., 2013; Shibazaki et al., 2016; Nishihara et al., 2012; Shibazaki et al., 2020; Funamori et al., 1996; Anzellini et al., 2013; Komabayashi & Fei, 2010; Ohtani et al., 2013; Shahar et al., 2016; Sakai et al., 2014; Komabayashi et al., 2009; Yamazaki et al., 2012; González-Cataldo & Militzer, 2023; Kuwayama et al., 2020; Brown & Mcqueen, 1986; Brown et al., 2000; W. W. Anderson & Ahrens, 1994; Desai, 1986)

Acknowledgments

This work was supported by the National Key R&D Program of China (Grant No. 2021YFB3802300), the National Nature Science Foundation of China (Grant Nos. 12372370).

References

Alfè, D., Price, G. D., & Gillan, M. J. (2002, Apr). Iron under earth's core conditions: Liquid-state thermodynamics and high-pressure melting curve from ab initio calculations. *Phys. Rev. B*, *65*, 165118. Retrieved from `https://link.aps.org/doi/10.1103/PhysRevB.65.165118` doi: 10.1103/PhysRevB.65.165118

Anderson, O. L. (1986). Properties of iron at the earth's core conditions. *Geophysical Journal International*, *84*, 561-579. Retrieved from `https://api.semanticscholar.org/CorpusID:128695991`

Anderson, W. W., & Ahrens, T. (1994). An equation of state for liquid iron and implications for the earth's core. *Journal of Geophysical Research*, *99*, 4273-4284. Retrieved from `https://api.semanticscholar.org/CorpusID:27551780`

Anzellini, S., Dewaele, A., Mezouar, M., Loubeyre, P., & Morard, G. (2013). Melting of iron at earth's inner core boundary based on fast x-ray diffraction. *Science*, *340*, 464 - 466. Retrieved from `https://api.semanticscholar.org/CorpusID:31604508`

Brown, J. M., Fritz, J. N., & Hixson, R. S. (2000). Hugoniot data for iron. *Journal of Applied Physics*, *88*, 5496-5498. Retrieved from `https://api.semanticscholar.org/CorpusID:121588362`

Brown, J. M., & Mcqueen, R. G. (1986). Phase transitions, grüneisen parameter, and elasticity for shocked iron between 77 gpa and 400 gpa. *Journal of Geophysical Research*, *91*, 7485-7494. Retrieved from `https://api.semanticscholar.org/CorpusID:129107803`

Desai, P. D. (1986). Thermodynamic properties of iron and silicon. *Journal of Physical and Chemical Reference Data*, *15*, 967-983. Retrieved from `https://api.semanticscholar.org/CorpusID:95590422`

Dewaele, A., Denoual, C., Anzellini, S., Occelli, F., Mezouar, M., Cordier, P., … Rausch, E. (2015, May). Mechanism of the $\alpha - \epsilon$ phase transformation in iron. *Phys. Rev. B*, *91*, 174105. Retrieved from `https://link.aps.org/doi/10.1103/PhysRevB.91.174105` doi: 10.1103/PhysRevB.91.174105

Dewaele, A., & Garbarino, G. (2017). Low temperature equation of state of iron. *Applied Physics Letters*, *111*, 021903. Retrieved from `https://api.semanticscholar.org/CorpusID:103212786`

Dorogokupets, P. I. e. a. (2017). Thermodynamics and equations of state of iron to 350 gpa and 6000 k. *Scientific Reports*, *7*, 41863. doi: 10.1038/srep41863

Dziewoński, A. M., & Anderson, D. L. (1981). Preliminary reference earth model. *Physics of the Earth and Planetary Interiors*, *25*, 297-356. Retrieved from `https://api.semanticscholar.org/CorpusID:129232713`

Fei, Y., Murphy, C. A., Shibazaki, Y., Shahar, A., & Huang, H. (2016). Thermal equation of state of hcp-iron: Constraint on the density deficit of earth's solid inner core. *Geophysical Research Letters*, *43*, 6837 - 6843. Retrieved from `https://api.semanticscholar.org/CorpusID:132866914`

Foreman-Mackey, D., Hogg, D. W., Lang, D., & Goodman, J. (2013, March). emcee: The MCMC Hammer. , *125*(925), 306. doi: 10.1086/670067

Funamori, N., Yagi, T., & Uchida, T. (1996). High-pressure and high-temperature in situ x-ray diffraction study of iron to above 30 gpa using ma8-type apparatus. *Geophysical Research Letters*, *23*, 953-956. Retrieved from `https://api.semanticscholar.org/CorpusID:128619359`

González-Cataldo, F., & Militzer, B. (2023). Ab initio determination of iron melting at terapascal pressures and super-earths core crystallization. *Physical Review Research*. Retrieved from `https://api.semanticscholar.org/CorpusID:262178924`

Harris, C. R., Millman, K. J., van der Walt, S. J., Gommers, R., Virtanen, P., Cournapeau, D., … Oliphant, T. E. (2020, September). Array programming with

NumPy. *Nature*, *585*(7825), 357–362. Retrieved from https://doi.org/10.1038/s41586-020-2649-2 doi: 10.1038/s41586-020-2649-2

Hirose, K., Wood, B. J., & Voadlo, L. (2021). Light elements in the earth's core. *Nature Reviews Earth & Environment*, *2*, 645 - 658. Retrieved from https://api.semanticscholar.org/CorpusID:237272150

Ichikawa, H., Tsuchiya, T., & Tange, Y. (2014). The p-v-t equation of state and thermodynamic properties of liquid iron. *Journal of Geophysical Research: Solid Earth*, *119*, 240 - 252. Retrieved from https://api.semanticscholar.org/CorpusID:130604173

Johnson, P. C., Stein, B. A., & Davis, R. S. (1962). Temperature dependence of shock-induced phase transformations in iron. *Journal of Applied Physics*, *33*, 557-561. Retrieved from https://api.semanticscholar.org/CorpusID:120137987

Kaufman, L., Clougherty, E. V., & Weiss, R. J. (1963). The lattice stability of metals*iii*. iron. *Acta Metallurgica*, *11*, 323-335. Retrieved from https://api.semanticscholar.org/CorpusID:94888216

Komabayashi, T., & Fei, Y. (2010). Internally consistent thermodynamic database for iron to the earth's core conditions. *Journal of Geophysical Research*, *115*, 1-12. Retrieved from https://api.semanticscholar.org/CorpusID:54919859

Komabayashi, T., Fei, Y., Meng, Y., & Prakapenka, V. B. (2009). In-situ x-ray diffraction measurements of the γ-ϵ transition boundary of iron in an internally-heated diamond anvil cell. *Earth and Planetary Science Letters*, *282*, 252-257. Retrieved from https://api.semanticscholar.org/CorpusID:130768562

Kuwayama, Y., Morard, G., Nakajima, Y., Hirose, K., Baron, A. Q., Kawaguchi, S. I., … Ohishi, Y. (2020). Equation of state of liquid iron under extreme conditions. *Physical review letters*, *124 16*, 165701. Retrieved from https://api.semanticscholar.org/CorpusID:218562532

Labrosse, S. (2014). Thermal evolution of the core with a high thermal conductivity. *Physics of the Earth and Planetary Interiors*, *247*, 36-55. Retrieved from https://api.semanticscholar.org/CorpusID:122507563

Li, J., & Fei, Y. (2014). Experimental constraints on core composition.. Retrieved from https://api.semanticscholar.org/CorpusID:92064071

Li, J., Wu, Q., Li, J., Xue, T., Tan, Y., Zhou, X., … Sekine, T. (2020). Shock melting curve of iron: A consensus on the temperature at the earth's inner core boundary. *Geophysical Research Letters*, *47*. Retrieved from https://api.semanticscholar.org/CorpusID:225363462

Lindquist, B. A., & Jadrich, R. B. (2022). Uncertainty quantification for a multiphase carbon equation of state model. *Journal of Applied Physics*. Retrieved from https://api.semanticscholar.org/CorpusID:248331170

Liu, J., Lin, J., Alatas, A., & Bi, W. (2013). Sound velocities of bcc-fe and fe0.85si0.15 alloy at high pressure and temperature. *Physics of the Earth and Planetary Interiors*, *233*, 24-32. Retrieved from https://api.semanticscholar.org/CorpusID:21680558

Morard, G., Boccato, S., Rosa, A. D., Anzellini, S., Miozzi, F., Henry, L., … Torchio, R. (n.d.). Solving controversies on the iron phase diagram under high pressure. *Geophysical Research Letters*, *45*, 11,074 - 11,082. Retrieved from https://api.semanticscholar.org/CorpusID:92985762

Murphy, C. A., Jackson, J. M., & Sturhahn, W. (2013). Experimental constraints on the thermodynamics and sound velocities of hcp-fe to core pressures. *Journal of Geophysical Research: Solid Earth*, *118*, 1999 - 2016. Retrieved from https://api.semanticscholar.org/CorpusID:28881426

Nishihara, Y., Nakajima, Y., Akashi, A., Tsujino, N., Takahashi, E., Funakoshi, K., & Higo, Y. (2012). Isothermal compression of face-centered cubic iron. *American Mineralogist*, *97*, 1417 - 1420. Retrieved from https://api.semanticscholar.org/CorpusID:54601004

Ohtani, E., Shibazaki, Y., Sakai, T., Mibe, K., Fukui, H., Kamada, S., … Baron, A. Q. (2013). Sound velocity of hexagonal close-packed iron up to core pressures. *Geophysical Research Letters*, *40*, 5089 - 5094. Retrieved from https://api.semanticscholar.org/CorpusID:128586157

Sakai, T., Takahashi, S., Nishitani, N., Mashino, I., Ohtani, E., & Hirao, N. (2014). Equation of state of pure iron and fe0.9ni0.1 alloy up to 3mbar. *Physics of the Earth and Planetary Interiors*, *228*, 114-126. Retrieved from https://api.semanticscholar.org/CorpusID:129344647

Shahar, Anat, Murphy, Caitlin, Fei, Yingwei, … Yuki (2016). Thermal equation of state of hcp-iron: Constraint on the density deficit of earth's solid inner core. *Geophysical Research Letters*, *43*(13), 6837-6843.

Shibazaki, Y., Nishida, K., Higo, Y., Igarashi, M., Tahara, M., Sakamaki, T., … Ohtani, E. (2016). Compressional and shear wave velocities for polycrystalline bcc-fe up to 6.3 gpa and 800 k. *American Mineralogist*, *101*, 1150 - 1160. Retrieved from https://api.semanticscholar.org/CorpusID:101475614

Shibazaki, Y., Nishida, K., Tobe, H., Terasaki, H., & Higo, Y. (2020). Effect of hydrogen on the sound velocity of fcc-fe at high pressures and high temperatures.. Retrieved from https://api.semanticscholar.org/CorpusID:222954715

Singh, S., Briggs, R., Gorman, M. G., Benedict, L. X., Wu, C. J., Hamel, S., … Smith, R. F. (2023a). A structural study of hcp and liquid iron under shock compression up to 275 gpa.. Retrieved from https://api.semanticscholar.org/CorpusID:258180169

Singh, S., Briggs, R., Gorman, M. G., Benedict, L. X., Wu, C. J., Hamel, S., … Smith, R. F. (2023b). Structural study of hcp and liquid iron under shock compression up to 275 gpa. *Physical Review B*. Retrieved from https://api.semanticscholar.org/CorpusID:265190891

Sinmyo, R., Hirose, K., & Ohishi, Y. (2018). Melting curve of iron to 290 gpa determined in a resistance-heated diamond-anvil cell. *Earth and Planetary Science Letters*. Retrieved from https://api.semanticscholar.org/CorpusID:134890949

Stacey, F. D., & Davis, P. (2004). High pressure equations of state with applications to the lower mantle and core. *Physics of the Earth and Planetary Interiors*, *142*, 137-184. Retrieved from https://api.semanticscholar.org/CorpusID:129634838

Tateno, S., Hirose, K., Ohishi, Y., & Tatsumi, Y. (2010). The structure of iron in earth's inner core. *Science*, *330*, 359 - 361. Retrieved from https://api.semanticscholar.org/CorpusID:206528628

Waskom, M. L. (2021). seaborn: statistical data visualization. *Journal of Open Source Software*, *6*(60), 3021. Retrieved from https://doi.org/10.21105/joss.03021 doi: 10.21105/joss.03021

Yamazaki, D., Ito, E., Yoshino, T., Yoneda, A., Guo, X., Zhang, B., … Funakoshi, K. (2012). P-v-t equation of state for ϵ-iron up to 80 gpa and 1900 k using the kawai-type high pressure apparatus equipped with sintered diamond anvils. *Geophysical Research Letters*, *39*. Retrieved from https://api.semanticscholar.org/CorpusID:129695765

Zhang, J., & Guyot, F. (1999). Thermal equation of state of iron and fe0.91si0.09. *Physics and Chemistry of Minerals*, *26*, 206-211. Retrieved from https://api.semanticscholar.org/CorpusID:97322900

[Geophysical Research Letters]

Supporting Information for

Obtaining the Equation of State for Multiphase Iron under Earth's Core Conditions using Bayesian Statistics

Run Wu[1], Shikai Xiang[2*],YiSun[2*], Yunting Xian[3], Yin Luo[4] , Feifan Dai[5]

National Key Laboratory of Shock Wave and Detonation Physics, Institute of Fluid Physics

China Academy of Engineering Physics, Mianyang 621999, China

Contents of this file

Text S1. Bayesian Theory and Sampling

The two main differences between Bayesian and classical statistical methods are, firstly, that Bayesian methods consider the parameters in the model as random variables, and the random distribution of the parameters can be calculated by Bayesian formulas, and secondly, that Bayesian methods can take into account not only the sample information, but also the subjective a priori information of the parameters. Under the Bayesian framework, given the data and physical model, the probability of the parameters in the model can be expressed as:

$$p(\theta|data) = \frac{p(\theta)p(data|\theta)}{p(data)} \tag{1}$$

In the Bayesian framework, $p(\theta)$ represents the prior probability distribution of the parameter θ, reflecting the initial beliefs about the parameter before any experimental data is obtained. When there is little knowledge about the parameter, an uninformative prior such as a uniform distribution can be used. This type of prior assumes that within a specified interval, the likelihood of the parameter θ taking any value is the same. $p(data)$ denotes the probability distribution of the data, which is a normalization constant similar to the partition function in physics. This constant is necessary for sampling from the posterior distribution $p(\theta|data)$, but it does not directly affect the sampling process and therefore does not require special attention. $p(\theta|data)$ is the posterior probability distribution, describing the probability of the parameter θ after observing the experimental data. This distribution is obtained by updating the beliefs about the parameter through the combination of the prior distribution $p(\theta)$ and the likelihood function $p(\theta|data)$The likelihood function $p(data|\theta)$ represents the probability of observing the experimental data given the model parameters θ. It is commonly assumed that the error for a single data point follows a normal distribution, which means the likelihood function can be written as:

$$p(y_i|\widetilde{\mu_i};\sigma_i) = \frac{1}{\sqrt{2\pi}\sigma_i}e^{-\frac{(y_i-\widetilde{\mu_i})^2}{2\sigma_i{}^2}} \quad (2)$$

$$p(data|\theta) = \prod p(y_i|\widetilde{\mu_i};\sigma_i) \quad (3)$$

The uncertainty of a parameter is associated with the experimental data and its error and model. y_i is a single experimental data point, $\widetilde{\mu_i}$ represents the physical true value, and σ_i is the corresponding error. $\widetilde{\mu_i}$ is usually replaced by the parameter-containing physical model, $\mu(\theta)$, in performing the uncertainty quantification, and thus σ_i should contain the model error, the experimental measurement error, and the random error. The model error we consider negligible if the model is sufficiently correct and reasonable. Under the assumption that the experimental data points are all considered to be independent, the total calibration data likelihood function $p(data|\theta)$ is the product of the likelihood functions of a series of individual calibration data points.

The above describes the calculation of the posterior distribution of the parameters in the model, i.e., the parameter uncertainty, in the case of a physical model with given calibration data. Usually for parameter uncertainty quantification, it is implemented by sampling the Markov-chain Monte Carlo (MCMC) method. In this work, we use the python-emcee package to sample from the posterior distribution $p(\theta|data)$, which has been used many times in published projects in many astrophysical neighborhoods. emcee is computationally much more efficient and convergent than the standard MCMC method (Metropolis–Hastings) for sampling complex distorted probability distribution functions, due to the use of affine transformation model, which also conveniently allows multi-core CPUs to execute it in parallel.

Text S2. Treatment of Phase Boundaries

When dealing with multi-phase equations of state, the best way is to use the piece of data on the phase boundary to constrain the parameters in the model. Since the experimental data we generally measure are the two experimental variables of pressure P, temperature T, the usual practice is to use the inverse solved $P(T)$ or $T(P)$ function based on the equality of Gibbs free energies of the two phases on the boundary, or the equality of pressures and temperatures, which need to be solved inversely, and then further adding this constraint to the calculation. Of course, there are other approaches, Beth A. Lindquista and Ryan B. Jadrich were doing a parametric uncertainty analysis of the equation of state for carbon, and they derived a probability from Boltzmann statistics that could turn the points on the phase boundary into a classification problem, again with good results. In our operation, since there are more phases of iron, we still used the coexistence line model, but we did not invert the solution to solve for the functional relationship between pressure and temperature, which would also reduce the time spent. Instead, we changed our vision and added the equation constraints to the Bayesian approach to perform it.

Admitting that the experimental data all obey a Gaussian distribution, the great likelihood estimation, weighted least squares, and the Bayesian maximum probability estimation without prior information to obtain the optimal parameters should be the same from the point of view of the calibration data for the model parameters. In computing the weighted least squares.

$$\prod p_{yi} = \prod \frac{1}{\sqrt{2\pi}\sigma_{yi}} e^{-\frac{\left(y_i-\mu(\theta,x_i)\right)^2}{2{\sigma_{yi}}^2}} \tag{4}$$

$$\sum \frac{\left(y_i - \mu(\theta, x_i)\right)^2}{2{\sigma_{yi}}^2} \tag{5}$$

x_i, y_i experimental measurements corresponding to the independent variable and the dependent variable measurements corresponding to it, the experimental data and the model if they can be perfectly matched, there is no error, the second equation above the experimental measurements substituted into the calculation should be 0. That is, if we write down $y_i - \mu(\theta, x_i) = 0$, then f_i= 0, if we consider that there error, then it is not 0. In fact, this means that the magnitude of the second equation above is able to reflect the magnitude of the difference between the computed value of the model (which can also mean or the magnitude of the difference between f_i and 0) and the experimental value. If we do some complicated mathematical deformation or calculation of the equation $y_i - \mu(\vec{\theta}, x_i) = 0$, to get another equation for example written as $F_i(y_i, \vec{\theta}, x_i) = 0$, similarly F_i will be constant equal to 0 when the experimental measurements are substituted into the calculation without taking any error into account, and if there is any more error, the experimental measurements substituted into the calculation F_i is not 0. Similarly the size of the difference between F_i and 0 reflects the size of the difference between the experimental calibration data and the model calculation. That is, the constraints on the parameters in the second equation above are equivalent to the weighted least squares between the lower $F_i$and 0, as follows:

$$\sum \frac{(F_i(y_i, \theta, x_i) - 0)^2}{2{\sigma_{Fi}}^2} \tag{6}$$

Analogously the likelihood function can be obtained as:

$$p_{Fi} = \frac{1}{\sqrt{2\pi}\sigma_{Fi}} e^{-\frac{\left(F_i(y_i, \vec{\theta}, x_i) - 0\right)^2}{2{\sigma_{Fi}}^2}} \tag{7}$$

For the consideration of which σ_{Fi}, to give a special example, $F_i(y_i, \vec{\theta}, x_i) = f_i = y_i - \mu(\theta, x_i)$, that is, there is no mathematical manipulation (identity operation) of the above equation of $y_i - \mu(\theta, x_i) = 0$, and obviously we only need to calculate σ_{Fi} by means of error transmission: $\sigma_{Fi} = \sigma_{fi} = \sqrt{(\frac{\partial f_i}{\partial y_i} \Delta y_i)^2} = \sigma_{yi}$ .Substituting these into p_{Fi}, we find that p_{Fi}=p_{yi}. We therefore generalize the idea a bit to fit the deformation of the equations, to compute σ_{Fi} by means of error transfer. in a way that is sufficient. This idea is equivalent to considering $F_i(y_i, \vec{\theta}, x_i)$ as still obeying a normal distribution, treating it as an indirectly measured quantity, and 0 as a model theoretical computational value, and so again correctly taking into account the uncertainty introduced by the experimental measurements.

The mathematical form of the physical model is deformed and still retains the important information before the deformation. The mathematical essence of this is that when performing Monte Carlo sampling, or weighted least squares, and given the parameter $\vec{\theta}$ (at this point you can think of $F_i(y_i, \theta, x_i)$ as an indirect measure of y_i) we are going to go ahead and calculate equation (4) or equation (5). However, our approach is to use equation (6) and equation (7) to replace the computation of equation (5) and equation (4). Probabilistically, the direct and indirect measures correspond to the same value of the random variable in the sample space, and must have $p_{Fi} = p_{yi}$, so this substitution is possible. However, we must be clear that for which $\sigma_{Fi}$is considered it is estimated by error transmission, strictly speaking $\sigma_{Fi} = \left|\frac{F_i(y_i,\theta,x_i)}{y_i-\mu(\theta,x_i)}\sigma_{yi}\right|$, so this estimate is quite conservative. Another point is that this is itself an optimization tool, and after the mathematical form is morphed, the objective function is transformed from f_i to F_i, and the problem of finding the extremes of equation (4) and equation (5) is transformed into the problem of finding the extremes of equation (7) and equation (6), resulting in the optimal parameters to be different from the original due to the fact that the estimation of σ_{Fi} is passed through the error, but is not rigorous (with respect to the specific mathematical form). Experimentally, however, this practice is common and still gives good estimates of σ_{Fi}.

When dealing with the EOS boundary problem, based on the equality of the two-phase Gibbs free energies, we do not have to invert the solution to obtain the $P(T)$ or $T(P)$ function. $F_i\left(y_i, \vec{\theta}, x_i\right)$ the corresponding function is the difference between the Gibbs free energies of the two neighboring phases $G_a\ (P_i, T_i)\ - G_b\ (P_i, T_i)$, with a, b marking the two neighboring phase regions, y_i, x_i corresponds to P_i, T_i. From $F_i\left(y_i, \vec{\theta}, x_i\right)$, y_i, x_i are of comparable status, and it might be possible to consider the error in both the independent and dependent variables by means of error transfer, but we only considered the error in the pressure data.

Additionally, concerning the constraints on the liquid shock temperature, one can resort to the Rankin-Hugoniot equation:

$$E_H(V_H,T_H) - E_0(V_0,T_0) - \frac{1}{2}(P_H + P_0)(V_0 - V_H) = 0$$

Here, $E, P, V, and\ T$ represent internal energy, pressure, volume, and temperature, respectively. Subscript H denotes a point along the Hugoniot curve, while subscript 0 indicates the initial state. However, the starting point for iron is the bcc structure, and we did not directly address the internal energy of bcc iron but started with the internal energy of liquid iron at the melting point, then subtracted the experimentally measured enthalpy difference (1.3 kJ/g) (Anderson & Ahrens, 1994) to determine $E_0(V_0,T_0)$ for bcc iron.

$$E_0(V_0,T_0) = E_{bcc}\left(\frac{1}{7.85\ g/cm^3}, 300\ K\right) = E_{liqiud}\left(\frac{1}{7.019\ g/cm^3}\ ,1811\ K\right) - 1.3\ kj/g$$

Substituting into the above Rankin-Hugoniot equation:

$$E_{liqiud}(V_H,T_H) - E_{liqiud}(\frac{1}{7.019}, 1811) + 1.3 - \frac{1}{2}(P_H + P_0)(V_0 - V_H) = 0$$

The left-hand side of the above equation can be considered an indirect measured quantity, and its error can be estimated using error propagation methods. Alternatively, without solving for the temperature explicitly, one can incorporate probabilistic constraints directly, thereby accelerating calculation speed.

Text S3. Quantitative Details of Implementation

There are some details that we must elucidate when sampling and quantifying the parameters in the equation of state of iron in a Bayesian framework:

First, In our research, we employed the equation of state model put forth by Dorogokupets et al., with the detailed aspects of this model accessible in pertinent literature. For body-centered cubic (bcc) structured iron, we specified a Curie temperature of 1043 K and assigned an average magnetic moment per atom of $B_0 = 2.22$; these values were considered fixed parameters and not subject to optimization within the model. Within the solid phase, we characterized the thermodynamic properties of each atom using a set of ten parameters. Recognizing the entropy change that occurs between the solid and liquid states, we incorporated an extra parameter when describing the liquid phase, thus necessitating the use of eleven parameters for the liquid phase representation. With the aim of ensuring that the model could relatively accurately describe the thermodynamic behavior of iron under high-temperature and high-pressure conditions, we designated the hexagonal close-packed (hcp) structure as the reference phase region where the potential energy is zero. Throughout the entire model development process, we refrained from introducing any additional empirical parameters. Consequently, the modeling endeavor encompassed a total of 40 parameters in aggregate. By synergistically leveraging these parameters, we aimed to construct a model that would precisely reflect the thermodynamic characteristics of iron, particularly under extreme conditions.

Second, In our study, due to the absence of specific prior knowledge regarding the model parameters, we opted for a general prior distribution—a uniform distribution—which served as a preliminary assumption for these parameters. To accelerate the sampling process and swiftly enter the burn-in period, we initially utilized the Python-emcee package to conduct sampling estimates on individual phases. This initial step provided us with a rough outline of the plausible parameter ranges. Subsequently, we took the high-probability sampled values obtained from this first stage as the starting inputs for the parameter chains across all four phase regions, thereby conducting joint quantitative sampling for all phases. Additionally, we also considered employing the parameter values derived from previous experimental research conducted by Dorogokupets et al. as the starting points for our sampling, further enhancing the effectiveness and reasonableness of the sampling procedure.

Third, In this work, we use the python-emcee package to sample from the posterior distribution $p(\theta|date)$, which has been used many times in published projects in many astrophysical neighborhoods. Emcee (Foreman-Mackey et al., 2013) is computationally much more efficient and convergent than the standard MCMC method (Metropolis–Hastings) for sampling complex distorted probability distribution functions, due to the use of affine transformation models, which also conveniently allows multi-core CPUs to execute it in parallel. I used the mixed sampling from the Python-emcee package for DEMove, and DIMEMove (Boehl, 2022) the ratio corresponding to the two types of moves is (0.5:0.5), because the hybrid moves are much better than the default ones. Regarding the convergence analysis of the sample chain, emcee authors give a conservative estimate of about greater than 50 times the autocorrelation time step, we sampled the samples obtained to calculate the autocorrelation time of 4,000 steps, a total of 200,000 steps of sampling.

Fifth, for the case on the boundary, our data for the hcp-liquid boundary comes from the article (Li et al., 2020), which has more accurate thermometry data relative to the others. For the fcc-hcp-liquid boundary the data comes from the article (Morard et al., n.d.). For the bcc-fcc, bcc-hcp, and bcc-liquid boundary data read from articles (O. L. Anderson, 1986; Kaufman et al., 1963; Johnson et al., 1962).

Text S4. Probability Distribution of Parameters and Correlation Coefficients Between Parameters

After obtaining the simulation results, the direct visualization of a 40-dimensional posterior distribution is inherently challenging; consequently, we leveraged the Python library Seaborn to plot kernel density estimates for each individual parameter's marginalized distribution, thereby depicting their probability density functions in the Fig.1 . Fig.2 this plot represents a symmetric correlation matrix of 40 parameters within a multiphase equation of state, where red signifies positive correlation and blue indicates negative correlation; the darker the color, the stronger the correlation. Most pairs of strongly correlated parameters are found within the same phase, as evidenced by the diagonal blocks, for instance, in the bcc phase, V_0 and K exhibit strong positive correlation, while in the hcp phase, K and V_0, as well as K' show marked negative correlations. However, there also exist noteworthy inter-phase relationships where some parameters display significant correlations across different phases. For example, it can be observed that the Einstein characteristic temperature parameter Θ_0 and the reference energy U_0share a positive correlation between the bcc and fcc phases. This could imply that data at phase boundaries link these parameters across phases. This scenario suggests that the model's parameters are not mutually independent. The dependencies among the parameters must be taken into account to accurately reflect the underlying relationships in the model. However, we obtained sample values through sampling. After plugging in 10,000 samples into the posterior probability function, we found the parameter values corresponding to the maximum value of the posterior function, which are treated as the Maximum Posterior Probability (MPP) estimates. These estimated values are listed in the following Table 1.

Table 1. Maximum Posterior Probability (MPP) estimate of 1000 sets of parameters.

	bcc	fcc	hcp	$liquid$
V_0 (cm^3/g)	0.1267473544	0.1239622495	0.1210535874	0.1424706171
$K_0(Gpa)$	163.66348004	147.24377837	156.07389919	78.950276587
K_0'	5.5060150605	4.5688650309	5.6782779899	6.0465579669
$\Theta_0(K)$	283.60896417	199.17877870	217.61535001	229.14705084
β	1.1348028698	-0.1632751972	-0.0509793421	0.3357194740
γ_0	1.6041671999	2.1364013187	2.0599424899	2.1744112631
γ_∞	-0.364118620	-0.4110305217	0.18389759162	-2.8865018184
$e_0(10^{-6}K^{-1})$	170.81443981	143.716252101	65.0590856591	172.22209539
m	1.9272464163	1.39424465306	-0.9874161768	2.0973388146
$U_0(kJ/g)$	-0.0960101266	-0.0060216531	0	2.0383567906
α				-1.9126697751

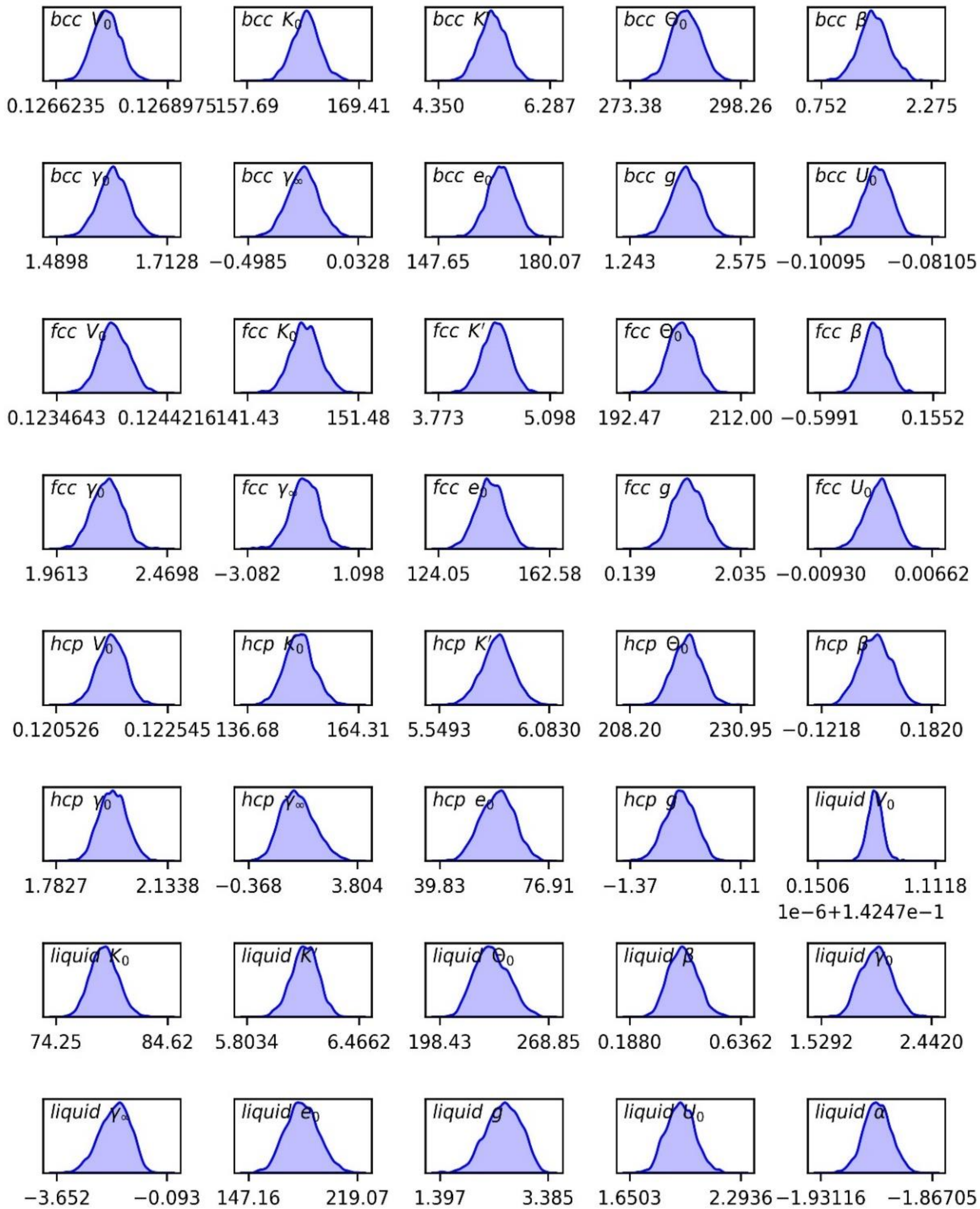

Figure 1. Plot kernel density estimates for each individual parameter's marginalized distribution for 40-dimensional parameters.

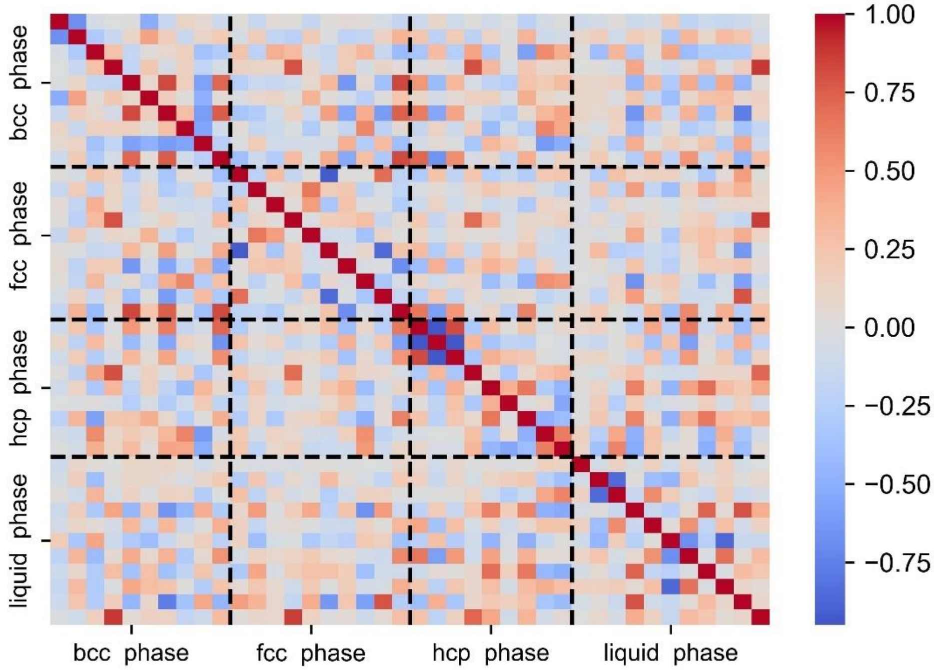

Figure 2. Correlation coefficients between 40-dimensional parameters in the multiphase equation of state for iron.

Text S5. Comparison of Computed and Experimental Values of Relevant Thermodynamic Quantities

The Fig.3 shows comparison of the calculated curve of heat capacity as a function of temperature under 0.1 MPa conditions with experimental data (Desai, 1986). It can be seen that our calculated results for the bcc structure are basically consistent with the experimental data , but the experimental data are significantly higher than our calculated data at the Curie temperature of 1043 K, which may be due to the fact that the mathematical model that describes the process of the ferromagnetic transition is still not precise enough. The calculated hot melt of the Fcc structure is in good agreement with the experimental data. of the heat capacity is in better agreement with the experimental data. The Fig.4 calculates the thermal expansion coefficients of iron in both bcc and fcc structures at a pressure of 0.1 MPa. The represent reference data (Novikova, 1974; Lu et al., 2005) from the article (Dorogokupets, 2017). As observed from the graph, the experimental data slightly exceed the calculated results, which may be due to the lack of experimental constraints on the thermal expansion coefficient for the fcc structure during the simulation process. The Fig.5 shows the comparison of the isothermal pressure lines calculated using

100 sets of parameters for solid phases with the corresponding experimental data. It can be seen that the calculation results can well reproduce the data for bcc-Fe, hcp-Fe at 15 K, bcc-Fe at 300 K, hcp-Fe at 300 K, fcc-Fe at 1073 and 1273 K (Nishihara et al., 2012). And like the melting curve, the uncertainty range of the calculated isothermal pressure lines is very small.

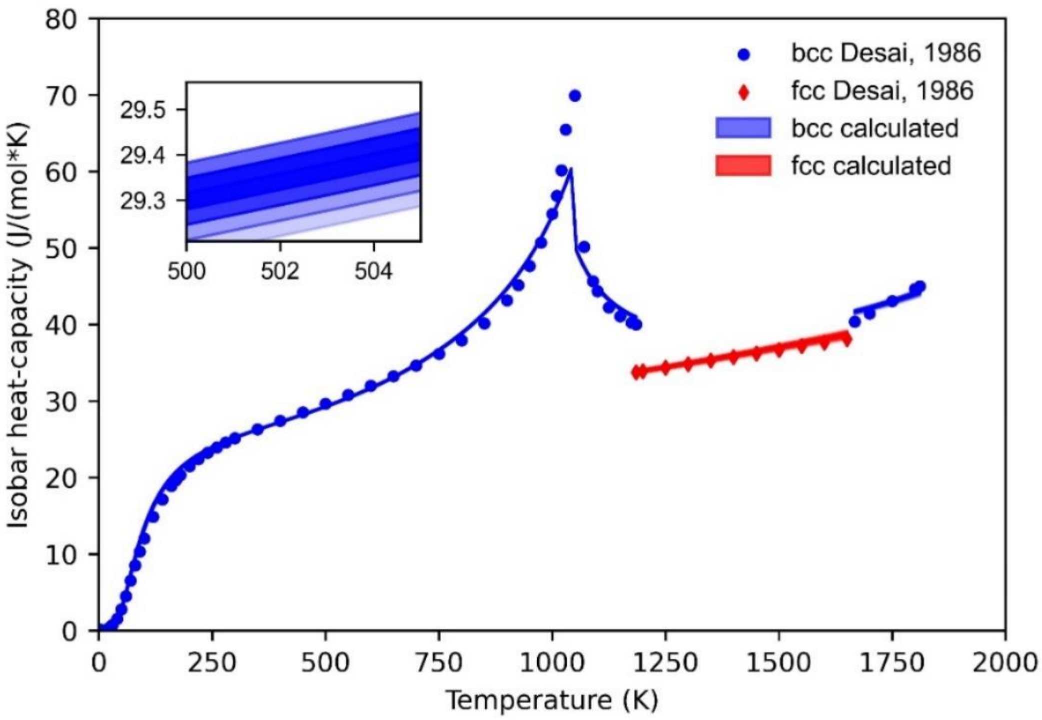

Figure 3. The figure illustrates the comparison of the calculated curve of heat capacity as a function of temperature at 0.1 MPa conditions using 100 sets of sample parameters against experimental data (Desai, 1986); only a portion of the experimental data is presented here.

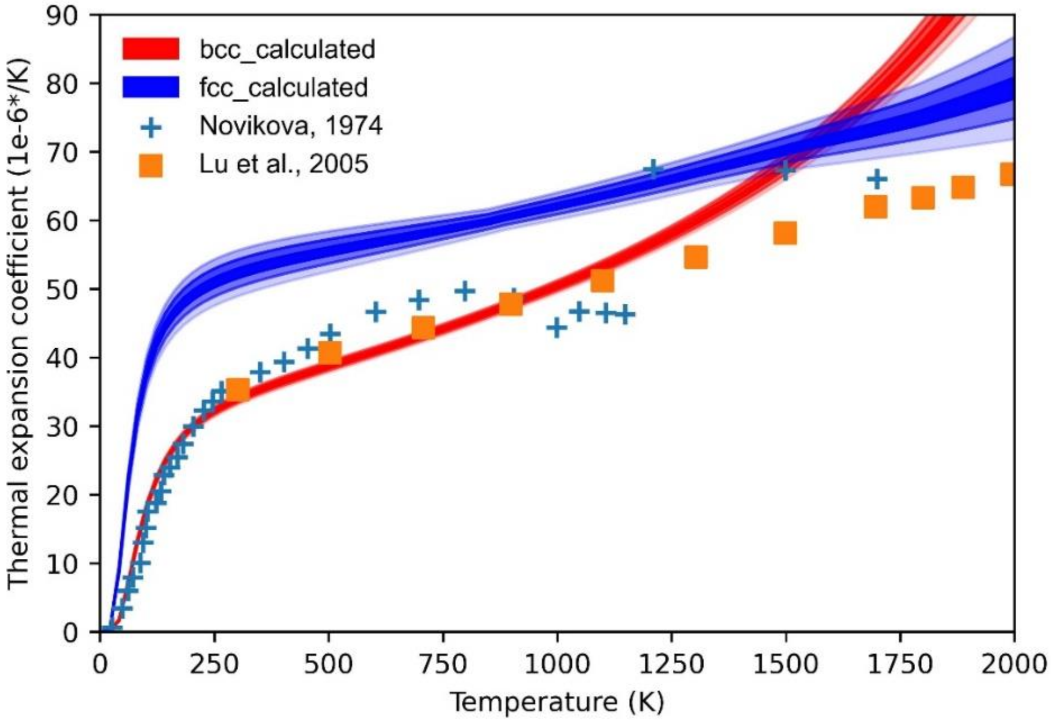

Figure 4. In this study, under 0.1 MPa conditions, the thermal expansion coefficients for bcc-Fe, fcc-Fe, and hcp-Fe structures have been calculated utilizing 100 sets of sample parameters. These computed results are intricately compared with the reference data furnished by Novikova (1974) and Lu et al. (2005), as illustrated within this figure.

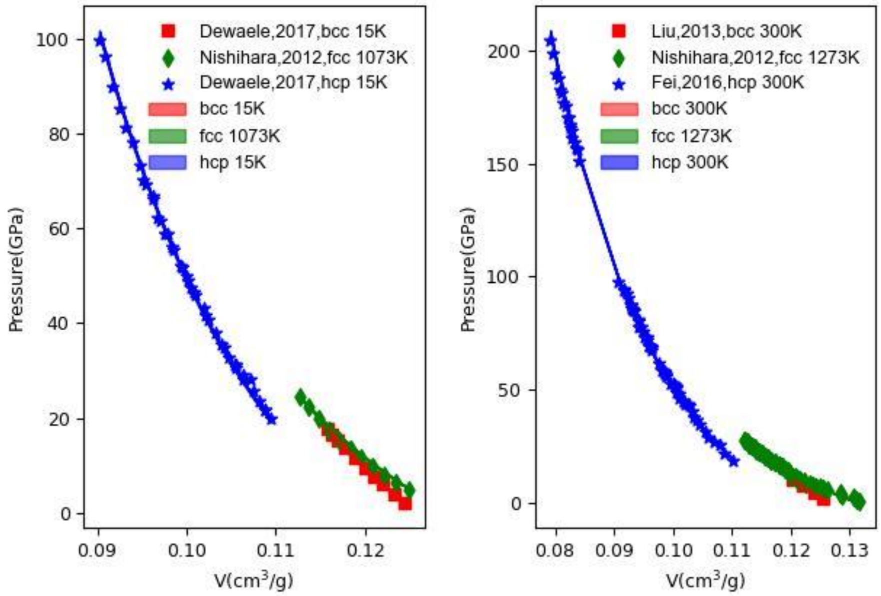

Figure 5. Comparison of the isothermal pressure lines calculated using 100 sets of parameters for solid phases with the corresponding experimental data (Dewaele & Garbarino, 2017; Liu et al., 2013; Nishihara et al., 2012; Fei et al., 2016)